Dynamic changes in mitochondria support phenotypic flexibility of microglia

Katherine Espinoza*[,1,2], Ari W. Schaler *[,1,2], Daniel T. Gray[1], Arielle Sass[1], Kamilia Moore[1], Megan Yu[1], Casandra Chamorro[1], Lindsay M. De Biase[1,3]

* Equal contribution
[1] Department of Physiology, David Geffen School of Medicine, UCLA, Los Angeles
[2] UCLA Neuroscience Interdepartmental Graduate Program
[3] Department of Neurobiology, David Geffen School of Medicine, UCLA, Los Angeles

Correspondence should be addressed to Lindsay M. De Biase at ldebiase@mednet.ucla.edu

ABSTRACT

The ability of microglia to sense the environment and alter their cellular phenotype according to local neuron and tissue needs is a hallmark feature of these cells. Numerous receptors that comprise the microglial “sensome” have been identified, but how microglia interpret combined signaling from diverse receptors and adjust multiple cellular attributes in a coordinated fashion is not well understood. Mitochondria are increasingly recognized as essential signaling hubs, and these organelles can regulate coordinated remodeling of cell attributes in immune cells, including macrophages. Given these findings, surprisingly little is known about microglial mitochondria *in vivo* and how the state of these organelles may impact microglial attributes and functions. Here, we generated novel transgenic crosses for high resolution analysis of microglial mitochondria in both fixed tissue and acute brain sections. Fixed tissue analysis indicated that mitochondrial abundance was tightly linked to microglial morphological complexity and that regional differences in microglial phenotype were accompanied by regional differences in mitochondrial mass and number. Surprisingly, multiphoton imaging revealed that mitochondrial abundance was not correlated with microglial cell process remodeling or rapid cell process extension toward focal sites of tissue injury. FACS- and qPCR-based analyses revealed remodeling of microglial mitochondrial state within hours of systemic LPS injections. Moreover, microglial expression of inflammation-, trophic-, and phagocytosis-relevant genes was strongly correlated with expression levels of numerous mitochondrial-relevant genes. Finally, FACS and fixed tissue imaging revealed that region-specific responses of microglia to aging were tightly linked to remodeling of these organelles. Overall, this study provides foundational information about microglial mitochondria and their relationship to differences in cell phenotype that occur across brain region, during pathological insults, and during aging. Moreover, these data demonstrate mitochondria support microglial phenotypic flexibility.

INTRODUCTION

An essential and defining characteristic of microglia is their ability to rapidly remodel their attributes and shift into different functional states(1–3). During embryonic and early postnatal development, microglia undergo extensive morphological and transcriptomic

changes as they support different phases of CNS maturation(4–9). In adulthood, microglia exhibit prominent regional differences in cell density, morphology, motility, and phagocytic behaviors to optimally support local neuron function and tissue homeostasis (10–15). Finally, microglia show dramatic alteration of numerous cell attributes as they respond to CNS challenges. This includes unique patterns of change in cell properties in response to everything from chronic stress, to high fat diet, to pollution exposure, to aging, to brain injury, and to disease(16–22). The ability of microglia to remodel their properties and acquire distinct cellular functional states plays a critical role in shaping neuronal health in all of these contexts.

Clearly a critical ingredient in microglial capacity to rapidly alter cellular phenotype rests on their ability to sense the local environment. Microglia possess an impressive repertoire of cell surface receptors that detect everything from ATP to pathogens to trophic factors (23–25). They also continually extend and retract their cell processes into the surrounding tissue (26–28), enabling dynamic and highly localized sensing of the surrounding environment. The field has elucidated how multiple cell surface receptors and associated intracellular signaling pathways can regulate key microglial properties and functions. These include P2RY12, TLR4, TGFBR2, CX3CR1, CR3 (ITGAM), and CSFR1, among many others. Yet, there are major gaps in our understanding of how microglia “interpret” simultaneous streams of information coming from distinct signaling axes and convert this into coordinated remodeling of multiple cell attributes to achieve the needed cellular phenotype in any given context.

Recent findings suggest that mitochondria may play an essential role in regulating coordinated changes in cell attributes. Classically thought of as the ATP producing “powerhouse” of the cell, mitochondria are now recognized as critical signaling hubs (29–32). Mitochondria influence intracellular signaling by buffering calcium, by providing metabolites needed for protein post-translational modifications, by interacting physically with other organelles, and by signaling to the nucleus to impact gene expression (29–32). Research in macrophages supports this view of mitochondria as signaling hubs, demonstrating that mitochondria regulate macrophage responses to pathology and shifts into distinct inflammatory states (33–39). Little is known about mitochondria in microglia *in vivo*. However, regional differences in microglial phenotype

are accompanied by prominent differences in expression of mitochondrial-relevant genes (40), and the state of mitochondria appears to be linked to microglial responses to early life immune challenge, brain injury, and protein aggregates in neurodegenerative disease (41–44). Given these intriguing observations, it is surprising how little is known about potential mitochondrial regulation of microglial attributes and phenotypic changes. In this study, we use novel transgenic crosses and multidisciplinary approaches to define for the first time the mitochondrial landscape within microglia *in vivo* and explore the relationship of these organelles to microglial phenotypic remodeling across brain regions, in response to inflammatory insult, and during aging.

RESULTS

Region-specific phenotypes of microglia are accompanied by regional differences in mitochondrial mass and number. Mitochondrial abundance, morphology, and molecular composition vary dramatically across cell types (45), arguing that findings about how these organelles impact cellular function cannot be generalized across cell types. Little is known about microglial mitochondria *in vivo*, in part because it is difficult to clearly identify these organelles with immunostaining approaches, which will label all mitochondria in all cells within the tissue. To enable clear visualization of microglial mitochondria *in vivo*, we crossed mice that express inducible cre recombinase in microglia (*CX3CR1*$^{CreER/+}$) with mice that express a mitochondrial-targeted GFP (*mitoGFP*) in Cre-dependent fashion (**Fig. 1A**)(46,47). In fixed tissue from young adult (2mo) double transgenic *CX3CR1*$^{CreER/+}$*;mitoGFP* mice (*MG-mitoGFP* mice), numerous GFP+ structures could be observed throughout the somas and cell processes of microglia (**Fig. 1B** and **Fig. S1A,B**) in multiple brain regions. Consistent with reports of tamoxifen-independent recombination when using *CX3CR1*$^{CreER/+}$ and reporter lines with minimal distance between loxP sites(48,49), significant recombination was observed in *MG-mitoGFP* mice without administration of tamoxifen. Quantification in fixed tissue from nucleus accumbens (NAc) and ventral tegmental area (VTA), two brain regions where microglia display distinct cellular phenotypes, revealed that roughly 60-85% of IBA1+ microglia contained GFP-tagged mitochondria in both brain regions (**Fig. S1A -**

C). Moreover, GFP-labeled structures were not observed outside of IBA1+ cells. Using flow cytometry to measure the percentage of GFP+ microglia in midbrain (containing VTA) and striatum (containing NAc), similarly indicated that approximately 80% of microglia were GFP+ even in the absence of tamoxifen injection (**Fig. S1D- F**). Flow cytometry also confirmed that other CNS cells were not GFP+ (**Fig. S1G**), validating cellular specificity of the mitochondrial reporter. Finally, to verify that GFP-tagged structures are mitochondria, we used tetramethylrhodamine (TMRM), a mitochondrial membrane potential indicator, to label mitochondria in acute brain sections from *MG-mitoGFP* mice and found that GFP+ structures were consistently colocalized with TMRM (**Fig. S1H-I**). Together these results indicate that *MG-mitoGFP* mice accurately reveal the *in vivo* distribution of microglial mitochondria.

To explore the relationship between mitochondrial networks and baseline structure of microglia in young adult mice, we carried out high resolution confocal imaging and 3D reconstruction of both microglia and their mitochondria in the NAc and VTA (**Fig. 1B** and **Fig. S2A**), where microglia show prominent differences in cell density, branching complexity, and gene expression (40). Consistent with previous findings, microglial tissue coverage in the NAc exceeded that observed in VTA (40) (**Fig. 1C**). 3D reconstruction of microglial mitochondria revealed that volume of individual mitochondria ranged from 1-40 μm^3, with an average volume of 3 μm^3 and an average max volume of 6 μm^3, and these measures were relatively consistent across NAc and VTA microglia (**Fig. S2C**). Aspect ratio and sphericity of individual mitochondria, which are measures of mitochondrial shape, were also consistent across NAc and VTA microglia (**Fig. S2B, D**). However, despite showing reduced tissue coverage, VTA microglia exhibited a greater number of mitochondria relative to cell volume, as well as a greater total mitochondrial volume relative to cell volume (mitochondrial mass) (**Fig. 1D, E**). Together, these observations indicate that regional differences in microglial cellular phenotype are accompanied by regional differences in mitochondrial metrics.

Mitochondrial number is correlated with morphological complexity of microglia, particularly in the VTA. Microglia continually survey the surrounding brain tissue and their capacity to carry out this function is influenced by cell branching and morphological

complexity. To explore how mitochondrial networks relate to microglial branching structure, we crossed *MG-mitoGFP* mice to *Ai14* reporter mice to drive cytosolic expression of TdTomato (TdTom) in microglia along with GFP tagging of microglial mitochondria (**Fig. 1A**)(46,47,50). In fixed tissue from young adult (2mo) triple transgenic *MG-mitoGFP;Ai14* mice, microglia that expressed only mitoGFP, microglia that expressed only TdTom, and microglia that were positive for both mitoEGFP and TdTom could be observed (**Fig. S1E**). In the absence of tamoxifen injection, incidence of mitoGFP+TdTom+ cells was low enough to allow rigorous and unequivocal reconstruction of the branching patterns of individual microglial cells, as well as their mitochondrial networks (**Fig. 1F**). Consistent with previous findings (40), VTA microglia exhibited lower total process length and fewer branch points than NAc microglia in young adult *MG-mitoGFP;Ai14* mice (**Fig. 1G,I**). The maximum number of intersections in Sholl analysis was also lower in VTA compared to NAc microglia (**Fig. 1H**). Sholl analysis revealed that the subcellular distribution of mitochondria within microglia follows branching complexity of the cell (**Fig. S2F, G**). For example, the number of microglial Sholl intersections reached a maximum around 20-25 μm from the cell soma in both the NAc and the VTA. Similarly, mitochondrial distribution followed a similar trend, with peak mitochondrial number occurring around 20 μm from the cell soma in both the NAc and the VTA (**Fig. S2F, G**).

Using linear regression to further probe links between morphological and mitochondrial features of microglia revealed several general trends. First, there were a greater number of significant or nearly significant associations between total *number* of mitochondria and morphological features of microglia than there were associations between total *volume* of mitochondria and morphological features of microglia (**Fig. 1J,K,L**). Second, there were a greater number of significant and nearly significant correlations between mitochondrial and morphological features of microglia within the VTA than in the NAc (**Fig. 1J,K,L**). Some observed relationships made intuitive sense. For example, increasing total cell process length was correlated with increased total volume of mitochondria (**Fig. 1L, and Fig. S2I**). Other observed relationships were more surprising. For example, both total number of branch points and maximum number of Sholl intersections were positively correlated with total mitochondrial number in VTA

microglia. Hence, for VTA microglia, the architecture of cell processes, rather than simply the total amount of cell processes, was related to mitochondrial number (**Fig. 1J, K,L**). Together these analyses suggest that microglial and mitochondrial morphology are correlated and that changes in microglial morphology are accompanied by remodeling of mitochondrial networks within these cells.

Mitochondrial number and mitochondrial motility are not aligned with microglial tissue surveillance. In addition to morphological structure, the dynamics of microglial cell process extension and retraction shapes their overall capacity to survey the local brain parenchyma (26,27). Continual morphological remodeling of microglia is assumed to be an energy intensive process. However, the relationship between microglial cell process motility and mitochondrial abundance and distribution has not been explored previously. To gain initial insight into the relationship between these organelles and microglial motility, we performed two-photon imaging in acute brain sections prepared from young adult (2-3mo) *MG-mitoGFP;Ai14* mice. In mitoGFP+TdTom+ microglia, we carried out simultaneous imaging of both microglial cell processes (TdTom) and mitochondria within these cells (GFP) and could observe motility of both (**Fig. 2A-C**). A combination of modified 3DMorph code, FIJI plugins, and Imaris were used to reconstruct cells and organelles and track motility of both over time. Microglia were imaged at least 60μm below the surface of the brain section and microglial motility (total process remodeling, normalized to cell area) was not correlated with time elapsed since preparation of brain sections (**Fig. 2D**). Moreover, motility was not substantially different between cells with fewer or greater number of Sholl intersections (**Fig. S3F**), suggesting that observed dynamics are not primarily driven by responses to brain slice preparation. Finally, the positive correlation we observed between total mitochondrial volume and Sholl intersections in fixed tissue was preserved in acute brain sections (**Fig. S3D**), indicating that this preparation is well suited for initial exploration of relationships between mitochondria and microglial cell structure and dynamics.

Microglial motility was similar across NAc and VTA microglia (**Fig. S3G**), implying that less of the surrounding tissue is surveyed during a given time interval in the VTA, as VTA microglia are less branched and have lower tissue coverage compared to NAc

microglia (**Fig. 1C, G-I**). Although VTA microglia showed greater mitochondrial mass and mitochondrial # compared to NAc microglia, there was no correlation between total mitochondrial volume and microglial motility in the VTA (**Fig. 2E**). In the NAc, there was a negative correlation, such that microglia with lower total mitochondrial volume showed greater cell process motility (**Fig. 2E**). These observations suggest that there is a more robust relationship between mitochondrial abundance and underlying cell morphology than with dynamic remodeling of that morphology. However, mitochondria are somewhat sparsely distributed throughout microglia, raising the possibility that there could be relationships between extremely local cell process motility and distance to the nearest mitochondrion. The functional state of the mitochondria (membrane potential, calcium concentration, etc) may also show stronger correlation with microglial motility that simple abundance of mitochondria.

Along those lines, mitochondria themselves are highly motile organelles and their trafficking and localization can impact key cellular functions such as synaptic plasticity in neurons (51–53). Microglial mitochondria exhibited numerous forms of motility that included “jitter,” more concerted directional movement, and occasional examples of fission and fusion (**Fig. 2F**). 3D reconstruction of mitochondria in Imaris and tracking across time revealed that mitochondrial network motility (total displacement over time) was similar in NAc and VTA microglia (**Fig. 2G,H**). Average displacement of mitochondrial movement was also similar in NAc and VTA microglia (**Fig. 2H-I**). Linear regression analyses indicated that there was no significant relationship between average and total mitochondrial motility and cell process remodeling of microglia in either the NAc or the VTA (**Fig. 2J-K**). This finding further reinforces the idea that mitochondrial abundance, distribution, and motility are not linked in any direct fashion to baseline microglial tissue surveillance. Nonetheless, additional future analysis will be needed to explore whether there are highly localized changes in cell process extension or retraction in the presence of a mitochondrial trafficking or fission/fusion event and how cell process motility relates to mitochondrial state (membrane potential, calcium concentration etc.).

Although time post-sectioning was not significantly correlated with microglial tissue surveillance, there were trends toward a relationship between time post

sectioning and mitochondrial motility in both the NAc and the VTA (**Fig. S3E**). This observation suggests that microglial mitochondria are sensitive to the evolving response of the tissue to brain sectioning and that this sensitivity is first detected as changes in organelle motility. Intriguingly, potential associations occurred in opposite directions across brain region, such that mitochondrial motility appeared to increase in NAc with greater time post-sectioning, and mitochondrial motility appeared to decrease in VTA with greater time post-sectioning. This observation raises the possibility that there are regional differences in microglial responses to brain sectioning and that divergent mitochondrial remodeling may play a role in regulating such regional differences in microglial response to brain sectioning.

Mitochondrial distribution is stable during early phases of microglial response to focal injury. The results described above suggest that mitochondrial abundance and mitochondrial motility are not strongly tied to baseline microglial tissue surveillance. In addition to homeostatic tissue surveillance, microglia exhibit rapid and robust cell process extension toward focal sites of CNS injury (26,54). To explore the relationship between mitochondria and this robust cell process extension, we imaged microglial processes and mitochondria before and after focal laser lesions. Consistent with previous findings in the field (55,56), microglia in acute brain sections from *MG-mitoGFP;Ai14* mice extended cell processes toward the site of focal laser lesion, contacting the lesion within 10-15min (**Fig. 3A-E**). Surprisingly, these rapidly extending cell processes did not contain any mitochondria and no mitochondria were trafficked into these lesion-responsive processes even 70min post-lesion (**Fig. 3A-E**). Moreover, there did not appear to be obvious changes in somatic mitochondria or redistribution of mitochondria in processes on the non-lesion side of the cell. These findings suggest that energy needed for this rapid injury-induced morphological remodeling does not require mitochondria to be precisely at the site of cell process extension and/or energy needed for this remodeling is generated from glycolysis. Future experiments using *in vivo* imaging will be needed to explore whether changes in mitochondrial distribution within injury responsive microglia emerge several hours post-lesion. Future experiments can also define whether changes in mitochondrial membrane potential, calcium

buffering, or production of reactive oxygen species occur during rapid microglial responses to injury.

Mitochondrial remodeling is evident at the earliest stages of microglial responses to inflammatory challenge. In addition to tissue injury, microglia exhibit rapid responses to pathogens and inflammatory signals related to infection (1,57,58). To further explore the role of mitochondria in microglial responses to pathological challenges, we used intraperitoneal (i.p.) injections of lipopolysaccharide (LPS), a component of the cell wall of gram-negative bacteria, which is widely used to model systemic inflammatory responses that accompany infection. Microglia respond to this challenge with prominent changes in gene expression that emerge within hours of LPS injection and changes in morphology and further changes in gene expression that emerge by 24-48 hours post-injection (59). *In vitro* studies indicate that mitochondrial structure and functional state are altered within microglia following LPS exposure (60–63) and, in macrophages, mitochondrial alterations play an essential role in enabling and regulating changes in macrophage attributes as they respond to inflammatory challenges (34–39,64,65).

To explore early and late responses of microglia and their mitochondria to inflammatory challenge *in vivo*, young adult (3-4mo) *MG-MitoEGFP* mice were given i.p. injections of saline or LPS and microglial gene- and protein- expression were analyzed 4hr or 24hr post injection via FACS and downstream qPCR (**Fig. 4A**). Microglia from both striatum (STR, containing NAc) and midbrain (MB, containing VTA) were collected to enable comparison of microglial responses across brain regions. Within 4hr of LPS challenge, qPCR analysis revealed that both STR and MB microglia exhibited prominent up-regulation of pro-inflammatory factors (*Il1β*, *Tnfα*), and downregulation of homeostatic microglial genes (*Tgfβ1*, *P2ry12*, *Cx3cr1*), consistent with numerous studies showing robust microglial responses to this type of pro-inflammatory challenge (59,66). Upregulation of genes associated with microglial phagocytic function (*Cd45*, *Itgam*) was evident by 24hr post injection (**Fig. 4B** and **Table S1, S2**). Overall, STR and MB microglia responded similarly to LPS challenge at the gene expression level, with

only *Cd45* and *Cd68* exhibiting significant differences across region in patterns of gene regulation.

Microglial expression of mitochondrial-function related genes was also altered at both 4hr and 24hr post injection (**Fig. 4B** and **Table S1, S2**). Within 4hr of LPS challenge, genes related to mitochondrial ROS handling (*Sod2*, *Cat*), mitochondrial fission (*Dnm1l*), and mitochondrial biogenesis (*Nrf1*) were significantly altered. Some of these gene expression changes were maintained into 24hr post injection (*Sod2, Dnm1l*), while others appeared more restricted to the 4hr time point (*Cat*, *Nrf1*). At 24hr post injection, prominent upregulation of electron transport chain component genes *Ndufa12* (Complex I), *Cox4i1* (Complex IV), and *Atp5d* (Complex V) emerged. Genes related to mitochondrial calcium handling (*Vdac1*, *Micu1*) were also significantly altered. Again, most gene expression changes were similar across STR and MB, with only *Micu1* displaying significant regional differences in expression pattern (**Fig. 4B** and **Table S1, S2**). Together these data indicate that numerous facets of mitochondrial function are remodeled during microglial responses to inflammatory challenge and that mitochondrial remodeling begins at the earliest stages of microglial responses to inflammatory challenge. These observations argue against the idea that mitochondrial largely occurs “posthoc,” after changes in microglial cellular function, to support the energetic demands of a new cellular state.

Consistent with the idea that mitochondrial state is intimately linked to microglial functional state during responses to inflammatory challenge, Principal Component Analysis (PCA) based solely on expression patterns of mitochondrial function-relevant genes can explain 64.7% of sample variation with the first 2 components and 81% of variation with the first 3 components (**Fig. S4A**). Moreover, 24hr post injection samples cluster away from Saline samples (**Fig. 4C**) and 4hr post injection samples are interspersed among Saline samples or skewed toward the 24hr samples. Hence, without even considering microglial inflammatory genes or homeostatic genes, microglia that are responding to LPS challenge can be clearly identified on the basis of their mitochondrial function profiles.

To further probe the relationship between mitochondrial state and key features of microglia as they respond to inflammatory challenge, we used linear regression

analyses to examine correlation between individual microglial-state and mitochondrial-state genes (**Fig. 4D** and **Table S3**). As STR and MB microglia exhibited similar patterns of gene expression changes following LPS challenge, samples from both regions were combined for these analyses. At 4hr post LPS, microglial pro-inflammatory genes *Il1β* and *Tnfα* showed significant correlation with mitochondrial biogenesis genes (*Nrf1*, *Tfam*), mitochondrial fusion and fission genes (*Mnf1*, *Dnm1l*) and the ROS handling gene *Sod2* (**Fig. 4D** and **Table S3**). Expression of homeostatic microglial genes *Cx3cr1* and *P2ry12* showed significant correlation with electron transport chain genes (*Cox4i1*, *Ndufa12*, *Sdha*) and mitochondrial biogenesis genes (*Nrf1*, *Tfam*, *Ppargc1a*) in saline treated animals. The majority of these correlations were lost at 4hr post LPS and correlations were instead observed with calcium handling gene *Vdac1* and ROS handling genes (*Sod2*, *Cat*, *Gpx1*) (**Fig. 4D** and **Table S3**). Although *Cx3cr1* and *P2ry12* showed similar patterns of gene correlations in saline treated animals and at 4hr post LPS, they differed at 24hr, with *Cx3cr1* again showing many of the correlations that were evident in saline treated animals and *P2ry12* largely maintaining the pattern of correlations observed at 4hr post LPS. Collectively, these findings indicate that multiple facets of microglial function beyond just production of pro-inflammatory factors are tightly associated with the status of microglial mitochondria. Moreover, *Cd68*, a key microglial lysosome gene, did not show significant correlations with expression of microglial pro-inflammatory factors *Tnfα* and *Il1β* and correlations with *Cx3cr1* and *Tgfβ1* were present but not modulated by LPS treatment (**Fig. S4B** and **Table S4**). Only *Cd45* and *P2ry12* showed correlations with *Cd68* that were gained and lost, respectively, as a function of LPS treatment. This analysis provides initial hints that mitochondria, as organelles, have a privileged relationship with microglial functional state during inflammatory challenge compared to other organelles such as lysosomes.

The qPCR-based analyses presented thus far show high sensitivity for detection of early changes in cell and organelle state following LPS challenge. However, not all transcript level changes are maintained at the protein level. As an initial approach for detecting changes in microglial mitochondria at the protein and functional level, we analyzed data recorded during FACS isolation of microglia. The intensity of GFP, driven by mitoEGFP and reflecting mitochondrial mass, showed large, significant increases at

24hr post injection in both the STR and MB, with hints of emerging increases at 4hrs post injection (**Fig. 4E, 4F**). In contrast, the intensity of TMRM, a dye that accumulates in mitochondria in a mitochondrial membrane potential dependent manner, decreased significantly at 24hr post LPS (**Fig. 4E, 4F**). These changes in mitochondrial mass and mitochondrial membrane potential were accompanied by significant protein-level increases in CD45 by 24hr in STR microglia. Similar trends in CD45 levels that did not reach significance were observed in MB microglia. Protein level expression of CX3CR1 and P2RY12 differed across region but not across treatment (**Fig S4C**). These data confirm that there are changes in mitochondrial state at the protein and functional level that are associated with changes in microglial protein-level expression.

Increased mitochondrial mass and mitochondrial elongation are associated with microglial responses to inflammatory challenge. To investigate how LPS challenge impacts microglial mitochondrial morphology and cellular distribution, we used immunostaining, confocal imaging, and 3D reconstruction in Imaris to analyze NAc and VTA microglial mitochondria in fixed tissue from 3-4mo *MG-MitoEGFP* mice (**Fig. 5A, Fig. S5A**). These experiments focused on 24hr post-LPS, as FACS analyses indicated that functional and protein-level changes in microglia and their mitochondria were most evident at this time point (**Fig. 4**). 3D reconstruction of both microglia and their mitochondria revealed significant increases in mitochondrial mass at 24hr post LPS injection (**Fig. 5B**), consistent with FACS-based analyses. No significant changes in mitochondrial number were detected (**Fig. 5C**) and, instead, microglial mitochondria showed significant elongation, as detected by increases in aspect ratio, a measure of the mitochondria's longest axis divided by its shortest axis (**Fig. 5D**). These observations suggest that increases in mitochondrial mass may be due to mitochondrial biogenesis, coupled with mitochondrial fusion. This would be consistent with qPCR-based increases in mitochondrial biogenesis factors *Nrf1* and *Tfam*, as well as the observation of tight correlation between mitochondrial fission/fusion factors (*Mfn1* and *Dnm1l*) and rapid pro-inflammatory responses of microglia to LPS challenge (**Fig. 4B,D**). In addition, elongation of mitochondria has been associated with increased capacity for oxidative phosphorylation (67,68), which would be consistent with the

qPCR-based observation of robust increases in electron transport chain components (*Ndufa12*, *Atp5d*, *Cox4i1*, *Sdha*) at 24hrs post LPS (**Fig. 4B**).

Collectively, these findings indicate that microglial mitochondria undergo extensive functional and structural remodeling as microglia are responding to inflammatory challenge. Moreover, multiple aspects of mitochondrial state are tightly correlated with key changes in microglial attributes during this response to LPS challenge. Finally, remodeling of mitochondria was detected at very early stages of microglial responses to LPS challenge, supporting the possibility that these organelles play an enabling and regulatory role in shaping microglial responses to this challenge.

Microglial mitochondria undergo age-related morphological and functional changes. Microglia exhibit numerous changes during aging, including altered morphology and inflammatory profile (18,69–71). Results described above indicate that there are key relationships between mitochondria and microglial morphology (**Fig. 1**) as well as inflammatory profile (**Fig. 4**). Changes in mitochondrial function during aging have been heavily implicated in CNS functional decline and risk for neurodegenerative disease (29,72,73). Similarly, aging-induced microglial changes have also been implicated in risk for neurodegeneration (18,19,69–71). Yet, almost nothing is known specifically about the status of mitochondria *in* microglia during aging in the absence of overt pathology.

We used immunostaining, confocal imaging, and 3D reconstruction in Imaris to analyze NAc and VTA microglial mitochondria in fixed tissue from middle age (12-13mo) and late middle age (16-18mo) *MG-MitoEGFP* mice (**Fig. 6A**), and compared them to microglial mitochondria in young adult (2-3mo) mice. With age, mitochondrial mass tended to increase, particularly in the VTA and significant increases in mitochondrial number were observed in both NAc and VTA microglia (**Fig. 6B**). VTA microglia also showed a trend toward decreased mitochondrial elongation at 12-13mo (aspect ratio, p=0.09, n.s.) and significant increases in mitochondrial elongation at 16-18mo compared to the other two ages (**Fig. 6B**). Within mouse comparisons using paired t-tests revealed that the elevated mitochondrial mass in VTA microglia relative to NAc microglia were no longer significant at 12-13mo and 16-18mo, likely due to increased

mouse to mouse variation (**Fig. 6C**). The elevated mitochondrial number in VTA microglia relative to NAc microglia, was no longer evident at 12-13mo and appeared to potentially be reversing itself by 16-18mo. Finally, while mitochondrial aspect ratio was similar across regions in 2mo mice and 12-13mo mice, an elevated aspect ratio (greater mitochondrial elongation) was evident in VTA relative to NAc microglia at 16-18mo (**Fig. 6C**). These findings indicate that microglial mitochondria undergo multiple age-related structural changes with both similarities and differences in these changes across brain region.

To probe the functional state of microglial mitochondria during aging, we analyzed wild type (WT) microglia from STR (containing NAc) and MB (containing VTA) using FACS-based approaches (**Fig. 6D**). Analysis of mitochondrial membrane potential using TMRM revealed that MB microglia exhibited slightly more depolarized mitochondrial membrane potential (lower TMRM intensity) than STR microglia in 2mo old mice. These regional differences grew larger in 12-13mo mice and even larger in 16-18mo mice. Across ages, both regions showed significant changes in mitochondrial membrane potential, with MB microglia showing significant depolarization in 12-13mo and 16-18mo mice compared to 2-3mo mice. Interestingly, STR microglia exhibited hyperpolarized mitochondrial membrane potential (higher TMRM intensity) in 12-13mo mice compared to 2-3mo mice. At 16-18mo, however, they showed depolarized mitochondrial membrane potential, similar to MB (**Fig. 6E**). Together, these findings indicate that the functional status of microglial mitochondria changes significantly during aging, with key differences across brain region. Moreover, they suggest that remodeling of mitochondrial status begins in middle age, which aligns with the period when VTA microglia begin to show key aging features (74). Collectively, these data support the possibility that this organelle plays a key regulatory role in shaping microglial responses to aging or promoting microglial age-related changes.

DISCUSSION

The underappreciated complexity of mitochondria.

Mitochondrial energy production is highly efficient, generating 32 molecules of ATP for every molecule of glucose, compared to the 2 molecules of ATP per glucose generated

by glycolysis. Mitochondria are also highly dynamic, showing distinct structure and capacity for ATP production depending on subcellular location (45,46,75). Although all cells contain mitochondria and all cells rely on ATP for ongoing function, there is growing appreciation that not all cells “utilize” their mitochondria primarily for generating ATP. Indeed, mitochondria play key roles in generating metabolites and reactive oxygen species (ROS) needed for post-translational protein modifications. They participate in calcium buffering and lipid metabolism and interact with and regulate other organelles such as endoplasmic reticulum, lysosomes, and lipid droplets. Mitochondria can also signal to the nucleus and impact gene expression. Accordingly, the mitochondrial field has moved well beyond viewing this organelle as an energy producer, and instead supports a model in which this organelle is a critical signaling and regulatory hub within the cell (29–32,76).

Multiple studies indicate that mitochondria *regulate* changes in cell function, rather than simply adjusting ATP output “posthoc” to meet energetic needs of a new functional state. For example, in neurons, mitochondria can regulate emergence of synaptic plasticity (45,75) and, in astrocytes, mitochondria can regulate morphological and functional maturation of the cell (75,77). Mitochondria can also regulate the inflammatory state of macrophages and capacity of these cells to rapidly adjust their cellular phenotype in response to various challenges (34–39,76). Given evidence that mitochondrial dysfunction is implicated in developmental delays, epilepsy, migraine, psychiatric disorders, aging, and risk for neurodegeneration (78,79), a better understanding of how mitochondria impact the function of specific CNS cell types should be a priority for the field. However, because mitochondrial structure and molecular composition vary widely across distinct cell types (45), findings about the functional roles of these organelles cannot be generalized and mitochondria need to be studied with cellular specificity.

Our study is one of the first to provide detailed information about microglial mitochondria *in vivo* and the relationship between these organelles and dynamic changes in microglial function and cellular phenotype. Our findings support the idea that mitochondrial function is distinct across CNS cell types. In astrocytes, mitochondria are extremely abundant and make up about 80% of the astrocyte volume in young adult

mice (77). This is quite different from what we observed in microglia, where mitochondria occupy about 8% of cellular volume. Qualitatively, our experiments using TMRM incubation in acute brain sections suggest that microglial mitochondria are less hyperpolarized than mitochondria of surrounding cells (Fig. S1H). Our findings also support the idea that individual mitochondria vary depending on subcellular location. We often observed very elongated mitochondria in microglial cell processes and more complex, network-like mitochondria in cell somas. TMRM intensity of cell process mitochondria also appeared lower than that of somatic microglial mitochondria (Fig. S1H). Finally, motility of mitochondria also differed depending on cellular compartment, with somatic mitochondria showing more “jitter” and cell process mitochondria being more likely to exhibit concerted trafficking in one direction or the other.

How does mitochondrial state relate to homeostatic microglial functions?

Previous studies have suggested that mitochondrial function in microglia changes in the context of disease, stress, and immune activation (41,42,56,60,80). Almost nothing is known, however, about how these organelles impact physiological functions of microglia. Through rigorous 3D reconstruction of mitochondria and cellular branching within individual microglia, we found key relationships between mitochondrial abundance and microglial morphology in young adult mice. Intriguingly, mitochondrial abundance was correlated with both total process length as well as branching complexity of microglia. Hence, even if microglia have fewer mitochondria than other CNS cells, our data suggest that these organelles are likely to be involved anytime that microglial branching structure needs to be altered. Our FACS-based analyses of key microglial genes and a panel of mitochondrial relevant genes also indicated that mitochondrial status is linked to cell surface expression of key microglial receptors. In young adult mice, expression of P2ry12, Cx3cr1, and Tgfβ1 were significantly correlated with expression levels of multiple mitochondrial genes involved in oxidative phosphorylation, calcium handling, and ROS handling.

Regional specialization of cellular phenotype is also a key feature of homeostatic microglia (10,14,15,40,81). We found previously that differences in cellular phenotype of VTA microglia, compared to microglia in other basal ganglia nuclei, were accompanied

by differences in expression of mitochondrial-relevant genes (40). This observation suggests that mitochondrial state may play a central role in regulating regional differences in microglial cellular phenotype. In this study, we confirm that regional differences in microglial phenotype are indeed accompanied by regional differences in mitochondria within these cells. Lower tissue coverage of VTA microglia was accompanied by elevated mitochondrial mass and mitochondrial number compared to NAc microglia. Whole cell reconstruction confirmed that VTA microglia have lower total process length, number of branch points, and number of Sholl intersections compared to NAc microglia. Yet, the VTA microglia showed a greater number of significant and nearly significant correlations between number of mitochondria and cellular morphological features. Finally, our FACS analysis indicated that midbrain microglia (containing VTA) from young adult mice had more depolarized mitochondrial membrane potential (lower TMRM intensity) compared to striatum microglia (containing NAc). Together, these observations indicate that differences in mitochondrial status are tightly linked to regional differences in microglial phenotype that are observed under physiological conditions.

One of the most surprising findings of our study relates to microglial cell process motility. Since the discovery of *in vivo* microglial tissue surveillance in 2005 (26,27), the dynamic behaviors of these cells have captivated the field. This continual morphological remodeling is assumed to be an energy intensive process. However, we did not find a strong correlation between microglial cell process remodeling and abundance of mitochondria within VTA microglia. Moreover, abundance of mitochondria was negatively correlated with microglial motility in the NAc, which seems highly counter intuitive if these organelles are providing a primary energy source for cell process remodeling. Future studies will need to investigate highly localized relationships between microglial filopodia and distance to nearest mitochondria and examine whether mitochondrial membrane potential or other features of mitochondrial state are linked to microglial motility.

In this study, we also provide the first analysis of mitochondrial motility within microglia. Mitochondria can alter their distribution within the cell, as well as undergo fission and fusion (52,82). Work in peripheral macrophages demonstrates that such

mitochondrial structural remodeling can regulate key cellular functions (34–39). We found that microglial mitochondria exhibit most of the same forms of dynamic remodeling described in other cell types. In both NAc and VTA microglia, we observed mitochondria that appeared to “jitter” in place, mitochondria that underwent elongation or shortening, mitochondria that underwent directional trafficking and, occasionally, mitochondria that underwent fission or fusion. Some of these dynamic changes in mitochondria were extremely rapid, and may not be fully captured when simultaneously acquiring full stacks of individual microglia. Future studies can focus on imaging of mitochondria only to more fully define the features of their motility. It is also worth noting that we occasionally observed mitochondrial movement that was driven by retraction of a microglial cell process that appeared to “pull” a mitochondrion along “passively,” creating another type of mitochondrial motility that is not likely to be observed in more stationary CNS cells. Our study explored how mitochondrial dynamics relate to microglial cell process remodeling, providing the first analysis of this type. At the level of individual cells, we did not observe any correlation between mitochondrial displacement and cell process motility, suggesting that mitochondrial trafficking to specific subcellular locations is not required for baseline microglial tissue surveillance. Future studies can determine whether there are relationships between specific types of mitochondrial remodeling (e.g. fission or fusion) and highly localized microglial cell process motility.

Do mitochondria regulate microglial responses to CNS challenge?

The discovery of microglial tissue surveillance was accompanied by the discovery of extremely rapid injury responses of microglia (26,27). Following focal tissue injury, nearby microglia extend multiple cell process toward the lesion and encapsulate the damaged tissue within 10-15min. The status of mitochondria during this prominent and rapid morphological remodeling of microglia has not been directly examined. Through simultaneous multiphoton imaging of microglial mitochondria and microglial cell processes, much to our surprise, we found that mitochondria are relatively stable within the cell, even as microglial processes are rapidly extended toward laser lesions. This observation demonstrates that trafficking of mitochondria into the extending processes is not required for this rapid injury response. This finding complements the recent

observation that microglia can still extend their processes toward a focal injury when oxidative phosphorylation is inhibited via glucose removal (56). Future studies can examine longer time points post-lesion to determine whether structural remodeling of mitochondria or substantial mitochondrial trafficking occurs. Future studies can also investigate whether there are relationships between mitochondrial capacity to produce ROS or buffer calcium and microglial cell process extension toward lesions.

Microglia also exhibit rapid responses to inflammatory insults (59,66). Systemically injected LPS does not cross the blood brain barrier, but does elicit robust pro-inflammatory responses in peripheral immune cells that then impact the brain (83–85). Protein-level increases in inflammatory cytokines such as TNFα and Il1β can be detected within the blood by 20min post-injection and are subsequently detected within the brain tissue at 1-4hrs post-injection. Once these inflammatory signals enter the brain, microglia rapidly alter gene expression, showing upregulation of *Tnfα* and *Il1β* (among other inflammatory factor) transcripts by 2-4 hours post-injection (59). Microglial responses to this insult continue to evolve with changes in cell morphology, protein-level expression of cell surface receptors, and cell proliferation becoming detectable at 24-48hrs post injection.

We found that increases in microglial *Tnfα* and *Il1β* mRNA detected at 4hrs post injection were accompanied by transcript-level changes in expression of multiple mitochondrial-relevant genes. Moreover, expression levels of *Tnfα*, *Il1β*, and *Cd45* in individual samples were significantly correlated with expression levels of mitochondrial-relevant genes at this 4hr time point. These included genes involved in mitochondrial fission and fusion, calcium handling, and ROS handling, in addition to genes involved in mitochondrial biogenesis and oxidative phosphorylation. These findings support the possibility that mitochondrial signaling functions influence key microglial attributes and suggest that these organelles are doing more than simply altering energy production to support a newly emerging cellular phenotype. Substantial changes in mitochondrial status continued to be evident in the later phases of microglial responses to inflammatory insult, with significant increases in mitochondrial mass and mitochondrial elongation at 24hrs post LPS injection. Moreover, in principle component analysis, microglia could be clustered solely on the basis of their mitochondrial relevant genes.

Together these data argue that capacity of microglia to remodel their mitochondria will have major implications for how effectively these cells respond to inflammatory challenges. Any mitochondrial dysfunction within these cells could exacerbate or hamper their ability to respond to insults.

Mitochondrial dysfunction is a hallmark of brain aging and multiple mutations that increase risk for neurodegenerative disease are in mitochondrial-relevant genes (29,72,73). Microglia undergo changes in morphology, motility, and gene expression during aging and they have also been strongly implicated in shaping risk for neurodegenerative disease (18,69–71). What happens to *microglial* mitochondria during aging? Is cognitive decline during aging and increasing risk for disease driven in part by mitochondrial changes in microglia and how this impacts microglial function? For the first time, we analyzed microglial mitochondrial status during aging and revealed that changes in mitochondrial number and morphology emerge in middle age, in alignment with our prior observation of changes in VTA and NAc microglial properties at this time point. We also observed key regional differences in mitochondrial properties across aging with mitochondrial elongation and loss of membrane potential being more prominent in VTA/MB compared to NAc/STR microglia. Together with our prior finding that VTA microglia exhibit early increases in proliferation and production of inflammatory factors during aging, this raises the possibility that regional differences in mitochondrial status critically shape local microglial responses to aging.

MATERIALS AND METHODS

Mouse lines.

C57Bl6 WT mice were obtained from the NIA Aged Rodent Colony and housed in the UCLA vivarium for at least one month before experiments. *CX3CR1* $^{CreER/+}$ mice were originally obtained from Jackson Labs (stock #025524) and subsequently maintained in our colony (47). *Rosa26-lsl-mito-EGFP* mice (*mitoEGFP* mice) were obtained from Dr. Jeremy Nathans (Johns Hopkins University) and are available at Jackson Labs (stock #021429). These mice enable cre-dependent expression of GFP that is fused to an N-terminal signal derived from mouse cytochrome c oxidase, subunit VIIIa, enabling specific localization to mitochondria (46). Ai14 td tomato reporter mice were obtained

from Jackson Labs (stock #007914) and subsequently maintained in our colony (50). Mice used for experiments were heterozygous for all transgenes. In all experiments balanced numbers of male and female mice were used. Mice were housed in normal light/dark cycle and had ad libitum access to food and water. All experiments were performed in strict accordance with protocols approved by the Animal Care and Use Committees at UCLA.

Lipopolysaccharide Injections.

CX3CR1 $^{CreER/+}$*; mitoEGFP* mice 3 to 5 months of age (mos) received single intraperitoneal injections of 1mg/kg of Lipopolysaccharide (LPS) (Millipore Sigma, strain O55:B5, L2880-25MG) or saline. All injections were performed around ~10am and mice were euthanized for immunohistochemistry or flow cytometry at 4 h or 24 h post-injection.

Tissue collection and immunohistochemistry.

CX3CR1 $^{CreER/+}$*; mitoEGFP* (postnatal day 60, 12-13mo, and 16-18mo) or *CX3CR1* $^{CreER/+}$*; mitoEGFP ; Ai14* (postnatal day 60) mice were deeply anesthetized via isoflurane inhalation and transcardially perfused with 1M phosphate buffered saline (PBS; pH 7.4) followed by ice-cold 4% paraformaldehyde (PFA) in 1M PBS. Brain tissue was isolated and postfixed PFS for ~4 h at 4°C and then stored in 1 M PBS with 0.1% sodium azide until sectioning. Coronal brain sections were prepared using a vibratome at 60 mm thickness. For immunostaining, free-floating brain sections were washed with 1M PBS (5 min) and then permeabilized and blocked in a solution of 2% bovine serum albumin (BSA) and 3% normal donkey serum (NDS) and 0.01% of Triton-X for 2 h with rotation at room temperature. Sections were then incubated overnight with primary antibodies prepared in 2% bovine serum albumin (BSA) and 3% normal donkey serum (NDS) at 4°C with rotation. Sections from aged mice were incubated in TrueBlack lipofuscin autofluorescence quencher, (5%; Biotium cat: 23007) for 60 s followed by a 3x5 min rinse in 1M PBS prior to incubation with primary antibodies. Following primary antibody incubation, sections were washed 3x with 1M PBS and then incubated with secondary antibodies prepared in 2% bovine serum albumin (BSA) and 3% normal donkey serum (NDS) at room temperature for 2 h with rotation. This was followed by washes in 1M

PBS (3x) with second wash containing 1:4000 dilution of DAPI in 1 M PBS. Sections were mounted using Aqua-Poly/Mount (Polysciences cat: 18606) and cover slipped (coverslips of #1.5 thickness). Primary antibodies used include rabbit anti- Iba1 (1:800; Wako, catalog #019-19741), rat anti-CD68 (1:200; clone FA11, AbD Serotec, catalog #MCA1957), chicken anti-TH (1:500; Aves, catalog #TYH). Secondary antibody combinations include rabbit AlexaFluor-647, chicken AlexaFluor-594, rat AlexaFluor-594, or chicken AlexaFluor-405 (used at 1:1000; all raised in donkey; Jackson ImmunoResearch Laboratories). For each set of analyses, three brain sections containing nucleus accumbens (NAc) and three brain sections containing ventral tegmental area (VTA) were chosen from each mouse. Brain sections were selected based on well-defined anatomical parameters and were matched for anterior-posterior location.

Confocal image acquisition and analysis.

Fixed tissue slides were imaged using a Zeiss LSM880 confocal microscope or a Zeiss LSM700 confocal microscope. Within the NAc, images were acquired at the boundary between core and shell (identified anatomically) and include both subregions. In the VTA, images captured were medial to the medial lemniscus. For quantification of MitoEGFP recombination within microglia, stacks of confocal images (z stacks) with a z interval of 1 μm were taken using a 20x objective and imported into ImageJ software for analysis. Maximum intensity projections were counted manually for the % of microglia exhibiting MitoEGFP expression. For 3D reconstruction of microglia and mitochondria, confocal z stacks were acquired with a 63x objective and z interval of 0.3 μm and imported into Imaris (Bit plane) software for analysis. The surface reconstruction module was used for quantification of mitochondrial and microglial volumes. For all image analyses, two or three images from separate brain sections were analyzed per mouse to obtain an average value for that mouse. Three to 7 mice were analyzed per brain region, per age and per condition. Sample sizes were selected to be in the upper range of published immunohistochemistry experiments. The filament tracer module was used for in depth analysis of microglial morphology, with 3 to 4 microglia from separate mice reconstructed per brain region. Surfaces were also created for mitochondria from filament-traced microglia to enable linear regression analyses.

Acute brain slice preparation.

Acute slices were prepared for ex-vivo two-photon microscopy. *CX3CR1* $^{CreER/+}$*; mitoEGFP* or *CX3CR1* $^{CreER/+}$*; mitoEGFP ; Ai14* mice at 1.5 to 2.5 months were anesthetized with isoflurane and perfused transcardially with 10 ml of oxygenated, ice-cold N-methyl-D-glucamine (NMDG)-based solution containing the following (in mM): 92 NMDG, 20 HEPES, 30 NaHCO3, 1.2 NaH2PO4, 2.5 KCl, 5 sodium ascorbate, 3 sodium pyruvate, 2 thiourea, 10 MgSO4, and 0.5 CaCl2, 10 glucose, pH 7.4 (310 mOsm). Brains were then rapidly dissected free and horizontal midbrain sections (230 mm thick) and coronal forebrain sections (300 mm thick) were prepared using a vibratome in ice cold NMDG-based cutting solution bubbled continuously with 95% O2/5% CO2. Following sectioning, sections were transferred to a holding chamber containing NMDG solution at 34 ^{o}C for 5 min and then transferred to artificial cerebrospinal fluid aCSF solution at room temperature for 30 min recovery containing the following (in mM): 125 NaCl, 2.5 KCl, 1.25 NaH2PO4 2H2O, 1 MgCl2 6H2O, 26 NaHCO3, 11 Glucose and 2.4 CaCl2 2H2O and bubbled continuously with 95% 02/5% CO2.

Acute brain slice multiphoton imaging.

Acute brain slices from NAc and VTA were imaged using a Leica Stellaris 8 Dive, multiphoton microscope equipped with a Coherent Chameleon Ultra II laser and a Leica 25x/1.00 NA W motCORR objective. During video acquisition, acute brain slices were continuously perfused with aCSF bubbled with 95% 02/5% CO2. Videos were acquired at least 60 µm below the surface of the slice and video acquisition was carried out 1-3 hours after sectioning. For analysis of microglial mitochondria only (*CX3CR1* $^{CreER/+}$*; mitoEGFP* mice) an excitation wavelength of 930 nm was used and EGFP was detected via a non-descanned detector (464 - 542nm). For analysis of microglial mitochondria and microglial cell process motility (*CX3CR1* $^{CreER/+}$*; mitoEGFP ; Ai14* mice) excitation wavelength of 930 nm was again employed, to maximize MitoEGFP signal and minimize TdTom signal bleaching. MitoEGFP and TdTom signals were detected via two non descanned detectors (detector 1: 463 – 537nm, detector 2: 558 - 668nm). Stacks of images encompassing entire microglial cells (z-step interval 1 µm) were acquired at 0.02Hz (for mitochondrial motility only) and .008Hz (mitochondrial motility + microglial cell process motility). To induce a focal laser lesion, exposure to high power illumination

of 750nm for 10 seconds was applied 60 μm below the surface in space surrounded by 4-5 cells. To achieve focal lesion, the zoom setting was set to max zoom available on the Leica Stellaris. Sections were imaged, zooming out of ROI to encompass 4-5 cells in the stack. Timepoints imaged post lesion included 10, 20, 50, 70 minutes. The excitation wavelength of 930 nm was again employed, to maximize MitoEGFP signal and minimize TdTom signal bleaching. MitoEGFP and TdTom signals were detected via two non descanned detectors (detector 1: 464 – 538nm, detector 2: 558 - 668nm).

Analysis of microglial and mitochondrial motility.

To analyze microglial motility, 3Dmorph, a previously published automated analysis pipeline by York et al., was adapted to analyze microglial motility (86). For microglial motility the Td Tomato channel was used. Movies corresponding to each cell underwent preprocessing through ImageJ using previously published methodology. The video underwent background subtraction, rolling ball radius 50, and applied a median filter. Then we performed z-stack projections of all movies and performed drift correction using the MultiStackReg ImageJ plugin. An ROI around the cell of interest was created based off a max projection of time for each cell and the signal outside of ROI was removed. The td tomato sparse labeling made it a clear method to isolate cells. The adapted 3D morph script was applied to the final 2D movie and collected pixels added/subtracted, total pixels changed, and microglial area change. To calculate microglial motility, the total number of pixels changed was collected and normalized to the total number of pixels in the cells (cell area), giving a quantification of motility normalized to cell size. All data was collected from the same elapsed time from all movies. To gain an understanding of the cell complexity, we used the Simple Neurite Tracer plugin in image j by Arshadi et al (87). Typically used for neuronal morphology but the sholl analysis plugin was used for microglial morphology. The same preprocessing as described previously was used, additionally for the sholl analysis the first and last frame of the frame of the movie were used and then the output values were averaged to obtain information of cell complexity. To analyze mitochondrial motility, the isolated MitoEGFP channel movie was used. The 3D movie was motion corrected and the ROI created based on the Td tomato signal was applied to the EGFP channel to isolate mitochondria for corresponding cell. The video was analyzed using Imaris (Bit

plane) Software. The surface reconstruction module was used to create surfaces for mitochondrial network across time frames. Editing of each surface track was performed to ensure the surface was accurately visualized across time. The measurements used were Displacement Length and Volume. A sum of these measures was taken per frame and subsequently averaged across the time intervals to achieve net displacement (the displacement was also divided by the time interval to achieve change over time) or total average volume.

Tissue dissociation and flow cytometry.

2-4mo, 12-13mo, and 16-18mo WT and *CX3CR1* $^{CreER/+}$*; mitoEGFP* mice were deeply anesthetized with isoflurane and transcardially perfused with 10 ml of chilled 1M PBS. The brain was rapidly removed, cut coronally with a razor blade using anatomical landmarks and midbrain and striatum were dissected free. Samples were thoroughly minced with razor blade on a chilled glass surface and transferred to 1.7mL tubes containing 1 mL Hibernate A Low-Fluorescence (Transnetyx Tissue, Half100). Samples were then mechanically dissociated using gentle sequential trituration with fire-polished glass pipettes of decreasing diameter. Cell suspensions were pelleted via centrifugation and resuspended in 1M PBS + Debris Removal Solution (Miltenyi, 130-109-398). Debris removal was carried out according to manufacturer's instructions. Following debris removal, samples were resuspended in small volumes of 1M PBS and incubated with primary antibodies on ice for 20min. Tetramethylrhodamine (TMRM) (Biotium, 70017) was used in some experiments to assess mitochondrial membrane potential. For these experiments, samples incubated with TMRM 50nM for 20 min at room temperature, prior to the antibodies step. Following incubation, samples were washed with 1xPBS and filtered through a 35mm filter (Falcon, 352235) prior to sorting.Throughout the experiment, samples were kept at 4°C on ice. Samples were sorted using a FACS Aria I cell sorter (BD Biosciences). The population of cells containing microglia could be readily identified based on forward scattering (FSC) and side scattering (SSC) properties. A gating strategy based on FSC and SSC width and height was used to select single cells and reduce dead cells and doublets. Microglial cells within this population were then identified and sorted based on combinations of microglial antibodies. Antibody combinations used included anti-CD45 (1:400; Biolegend, 147703),

anti-P2RY12 (1:500; Biolegend, 848005), and anti-CX3CR1 (1:800; Biolegend, 149023). Gated Microglia were FACS sorted into 1.7mL tubes containing 50µl Pico Pure RNA extraction buffer and, following the sort, samples were incubated at 42°C for 30 min, and stored in RNase-free tubes at -80°C until further processing.

RNA Extraction and qPCR.

Total RNA was extracted from sorted cells using Pico Pure RNA isolation kit (Arcturus Bioscience) according to the manufacturer's instructions. Single strand cDNAs were synthesized using Superscript III first-strand cDNA synthesis kit (Invitrogen, 18080051), according to the manufacturer's protocol. Samples were subjected to PreAmplification-RT-PCR method based on previously published approaches. TaqMan PreAmp Master Mix Kit was used for cDNA preamplification (Cat# 4391128; Applied Biosystems, Life Technologies), using pooled primer mixes of 20x dilution of TaqMan Gene Expression Assay and 80 nM of custom-designed primer sets. cDNAs were pre-amplified in an Veriti 96-Well Fast Thermal Cycler (ThermoFisher Scientific, 4375305) using the program: 95°C hold for 10 min, 14 cycles of 90°C denaturation for 15 s, and 60°C annealing and extension for 4 min. Pre-amplification PCR products were immediately diluted five times with molecular biology grade water and stored at -20°C, or immediately processed for RT-PCR. For qPCR analysis of gene expression, single plex qPCR assays were performed on technical duplicates using TaqMan probes for each gene target or for endogenous control gene (*Gapdh*). TaqMan Advanced Fast PCR Master Mix was used (catalog #4444963; Invitrogen). To avoid amplification of any genomic DNA contamination, primers and probes that amplify across target gene exon–exon junctions were selected when possible. qPCRs reactions were run in a QuantStudio5 using the program: 95°C hold for 20 s, followed by 40 cycles of 95°C denaturation for 3 s, and 60°C annealing and extension for 30 s. Calculations of relative expression from Ct data were conducted according to User Bulletin #23898 for ABI Prism 7900 Sequence Detection System. For each target gene, the average Ct value for the endogenous control (*Gapdh*) was subtracted from the average Ct value for the TaqMan Probe per target gene, to obtain DCt. The relative expression was then plotted

as 2^{-DCt}. All TaqMan Assays and custom primers/probes that were used are detailed in Table S5.

Statistical analyses.

Data analysis was performed in OriginPro and R. Heatmaps were generated in R using the ComplexHeatmap package by Gu Z et al (88). PCAs were generated in R using the ggplot2 package by Wickham H, 2016 (89). Linear regression analysis for LPS experiments were performed in R, all other linear regression analysis was performed in OriginPro. All graphed values are shown as mean ±SEM. Statistical details of experiments (statistical tests used, exact value of n, what n represents) can be found in Results and the figure legends. In general, statistical significance was assessed using one- or two-way ANOVA. Post hoc comparisons were conducted using Student's t test with Bonferroni correction for multiple comparisons. Data are sufficiently normal and variance within groups is sufficiently similar for use of parametric tests. 2 tailed paired t tests were used to compare trends across two different regions within individual mice.

FIGURES AND FIGURE LEGENDS
FIGURE 1

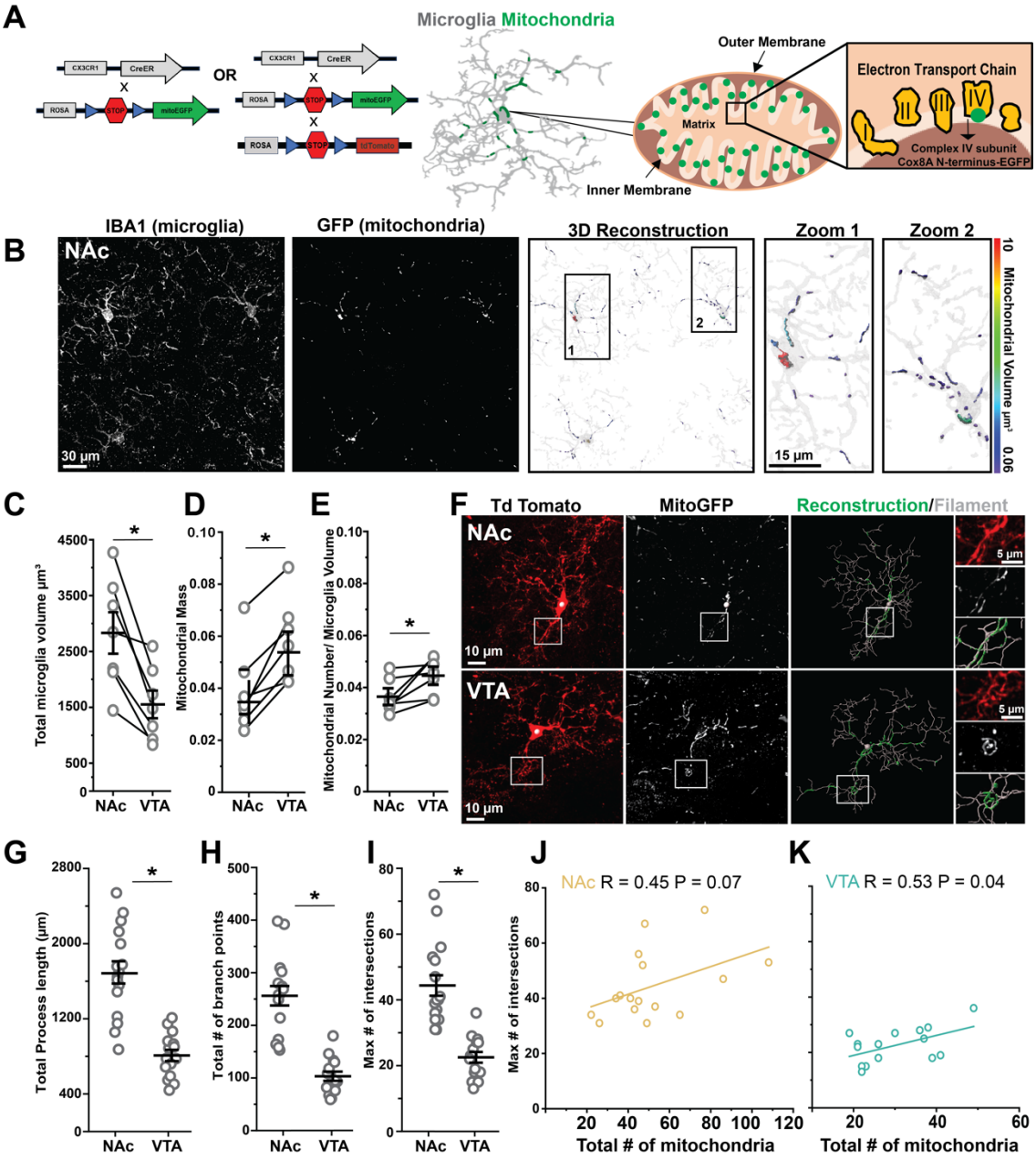

L

Morphological Parameters	Region	Total # of Mito	Total Vol. of Mito (µm³)
Total Process Length (µm)	NAc	R=0.14 P=0.59	*R=0.49 P=0.05*
	VTA	**R=0.48 P=0.06**	**R=0.44 P=0.09**
# of microglial branch pts.	NAc	R=0.13 P=0.61	**R=0.45 P=0.07**
	VTA	*R=0.56 P=0.02*	**R=0.49 P=0.06**
Max # of intersections	NAc	**R=0.45 P=0.07**	R=0.34 P=0.19
	VTA	*R=0.53 P=0.04*	R=0.43 P=0.10

FIGURE 1: Regional specialization of microglia is accompanied by regional differences in mitochondrial mass and number. (A) Schematic of transgenic crosses used to achieve GFP labeling of microglial mitochondria. **(B)** Representative high-magnification images at P60 of NAc microglia (Iba1) and mitochondria (GFP); panels *at right* show 3D reconstructions of microglia (*transparent gray*) and mitochondria (colored according to volume). **(C-E)** Quantification of microglia volume (tissue coverage), mitochondrial mass (mitochondrial volume / microglial volume), and mitochondrial number (relative to cell volume) in NAc and VTA. Data points from the same mouse are identified by the connecting line. * $p < 0.03$, paired t-test. **(F)** Representative confocal images of microglial cells in NAc and VTA expressing cytosolic TdTom and mitochondrial targeted GFP (*MG-mitoGFP;Ai14* mice). Reconstruction of cell branching via filament-tracing in Imaris along with 3D reconstruction of mitochondria is shown *at right*. **(G-I)** Morphological parameters individual microglia derived from filament tracing and Sholl analysis. * $p<0.0001$, two-sample t-test. (N=16 NAc microglia and N=15 VTA microglia). **(J-K)** Linear regression plots showing relationships between mitochondrial number and microglial morphological complexity as measured by max # of Sholl intersections. **(L)** Table containing statistics for all linear regression analyses performed.

FIGURE 2

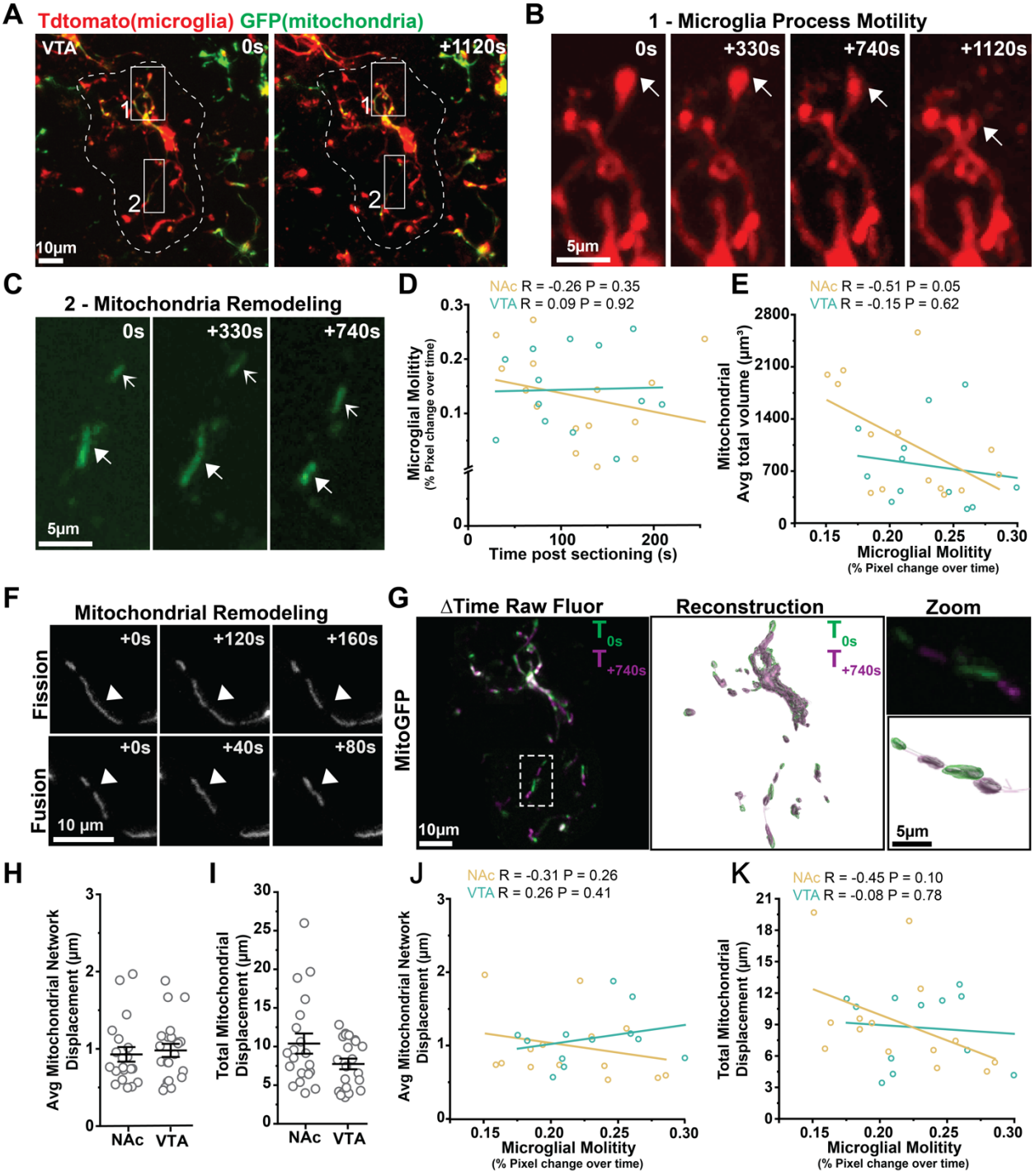
A
Tdtomato(microglia) GFP(mitochondria)
VTA
0s
+1120s
1
2
10µm
B
1 - Microglia Process Motility
0s
+330s
+740s
+1120s
5µm
C
2 - Mitochondria Remodeling
0s
+330s
+740s
5µm
D
NAc R = -0.26 P = 0.35
VTA R = 0.09 P = 0.92
Microglial Molitity
(% Pixel change over time)
Time post sectioning (s)
E
NAc R = -0.51 P = 0.05
VTA R = -0.15 P = 0.62
Mitochondrial
Avg total volume (µm³)
Microglial Molitity
(% Pixel change over time)
F
Mitochondrial Remodeling
Fission
+0s
+120s
+160s
Fusion
+0s
+40s
+80s
10 µm
G
ΔTime Raw Fluor
Reconstruction
Zoom
MitoGFP
T0s
T+740s
10µm
5µm
H
Avg Mitochondrial Network
Displacement (µm)
NAc
VTA
I
Total Mitochondrial
Displacement (µm)
NAc
VTA
J
NAc R = -0.31 P = 0.26
VTA R = 0.26 P = 0.41
Avg Mitochondrial Network
Displacement (µm)
Microglial Molitity
(% Pixel change over time)
K
NAc R = -0.45 P = 0.10
VTA R = -0.08 P = 0.78
Total Mitochondrial
Displacement (µm)
Microglial Molitity
(% Pixel change over time)

FIGURE 2: Mitochondrial abundance and mitochondrial motility are not strongly correlated with microglial tissue surveillance. (A) Representative images of multiphoton live imaging of VTA microglia (Td Tomato) and their mitochondria (GFP) in acute brain sections from 1.5-2mo old mice. **(B)** Example of microglial cell process retraction indicated by *white arrow*. **(C)** Example of microglial mitochondria showing trafficking (*small arrowhead*), and elongation followed by shortening (*white arrow*). **(D)** Linear regression analysis of microglial motility (% pixel change over time) and time elapsed since preparation of acute brain sections. **(E)** Linear regression analysis of relationships between mitochondrial volume (total volume in cell averaged across time points to account for dynamic changes in mitochondrial volume) and microglial motility. **(F)** Representative examples of mitochondrial fission and fusion observed in microglia from young adult mice. **(G)** Raw fluorescence from multiphoton imaging (*left*) and 3D reconstruction of microglial mitochondria (*right*) colored by time. **(H-I)** Quantification of avg mitochondrial displacement and total mitochondrial displacement in NAc and VTA microglia. ($p=0.684$ *n.s.* for avg. mitochondrial displacement, and $p=0.07$ *n.s.* for total mitochondrial displacement, two sample t-test). (**J-K**) Linear regression analysis of relationships between avg mitochondrial network displacement and total mitochondrial displacement versus microglial motility for NAc and VTA microglia (N=14 NAc microglia and N=12 VTA microglia).

FIGURE 3

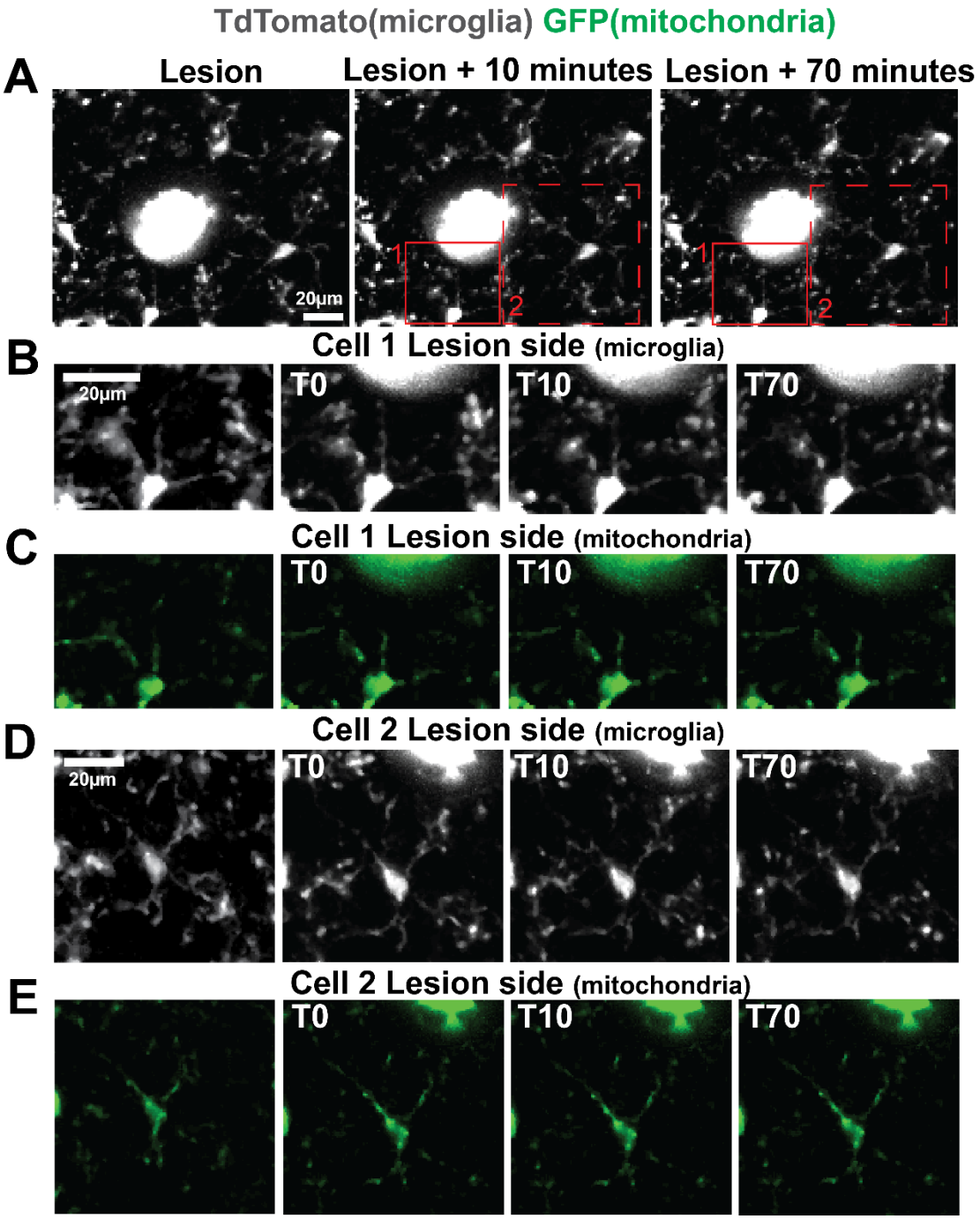

FIGURE 3: Mitochondrial distribution is stable during early phases of microglial response to focal injury. **(A)** Representative video of microglia in an acute brain slice from young adult *MG-mitoGFP;Ai14* mouse responding to focal laser lesion. **(B-E)** Higher magnification images of two microglia that extend cell processes toward the lesion while their mitochondrial networks (GFP) remain stable.

Figure 4

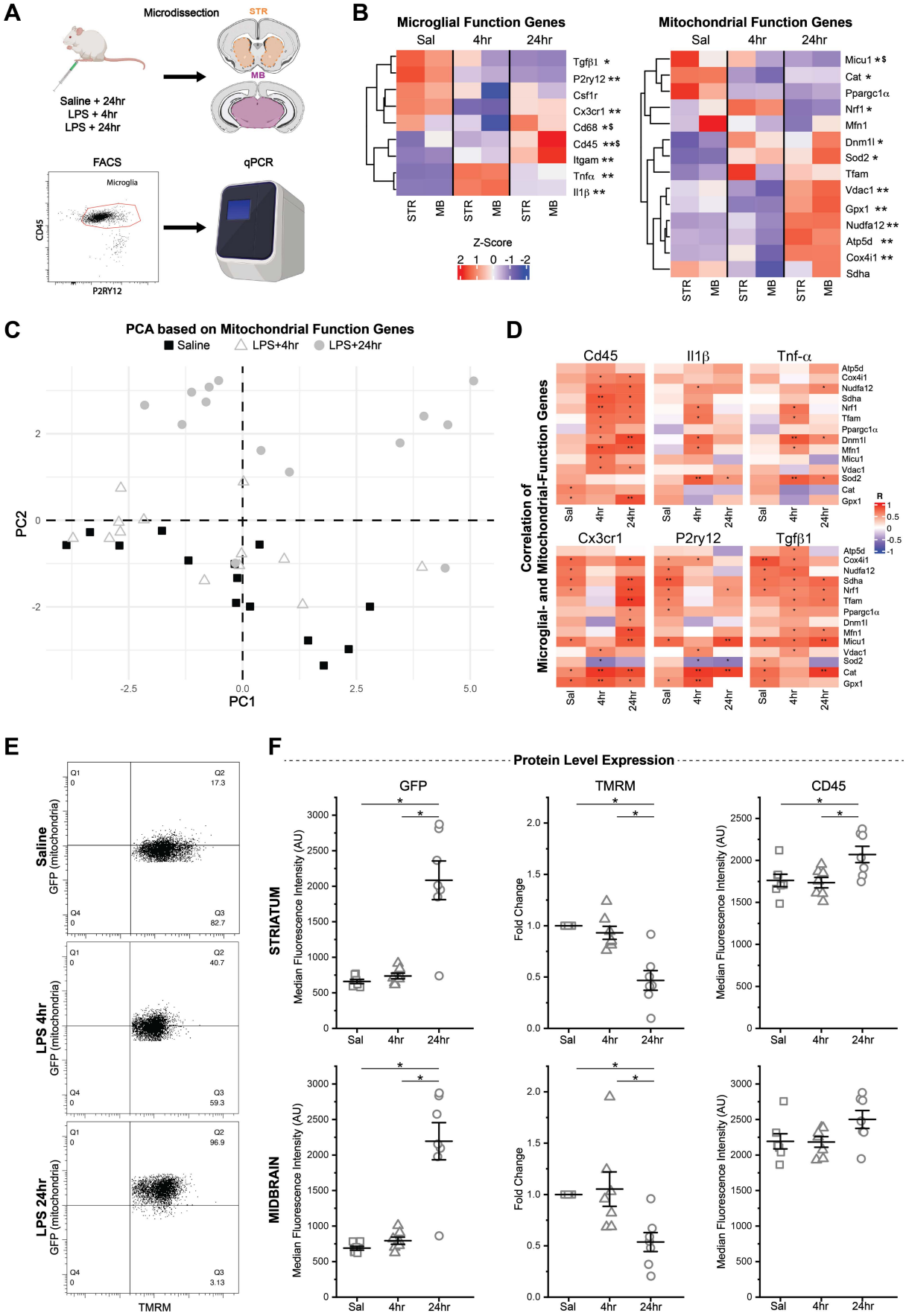
A
Microdissection
STR
MB
Saline + 24hr
LPS + 4hr
LPS + 24hr
FACS
Microglia
CD45
P2RY12
qPCR
B
Microglial Function Genes
Sal
4hr
24hr
Tgfβ1 *
P2ry12 **
Csf1r
Cx3cr1 **
Cd68 *$
Cd45 **$
Itgam **
Tnfα **
Il1β **
STR
MB
Z-Score
2 1 0 -1 -2
Mitochondrial Function Genes
Micu1 *$
Cat *
Ppargc1α
Nrf1 *
Mfn1
Dnm1l *
Sod2 *
Tfam
Vdac1 **
Gpx1 **
Nudfa12 **
Atp5d **
Cox4i1 **
Sdha
C
PCA based on Mitochondrial Function Genes
Saline
LPS+4hr
LPS+24hr
PC2
PC1
D
Cd45
Il1β
Tnf-α
Cx3cr1
P2ry12
Tgfβ1
Correlation of
Microglial- and Mitochondrial-Function Genes
Atp5d
Cox4i1
Nudfa12
Sdha
Nrf1
Tfam
Ppargc1α
Dnm1l
Mfn1
Micu1
Vdac1
Sod2
Cat
Gpx1
R
Sal
4hr
24hr
E
Saline
LPS 4hr
LPS 24hr
GFP (mitochondria)
Q1
Q2
Q3
Q4
17.3
82.7
40.7
59.3
96.9
3.13
TMRM
F
Protein Level Expression
GFP
TMRM
CD45
STRIATUM
MIDBRAIN
Median Fluorescence Intensity (AU)
Fold Change
Sal
4hr
24hr

Figure 4: Response to inflammatory challenge (LPS) elicits rapid mitochondrial changes in microglia. (A) Schematic of experiment design. 3-4mo *MG-MitoEGFP* mice were injected with saline 24hr prior to or LPS 4hr or 24hr prior FACS isolation of STR/MB microglia for downstream qPCR analysis. **(B)** Heatmaps showing expression levels of key microglial function and mitochondrial function genes in each group. Z-scores represent average gene expression across treatment groups and brain regions. See *Tables S1* and *S2* for F- and P-values. (N = 7 Saline STR, N = 7 Saline MB, N = 7 LPS 4hr STR, N = 6 LPS 4hr MB, N = 7 LPS 24hr STR, N = 7 LPS MB). **(C)** PC1 and PC2 of Principal Component Analysis of samples using only mitochondrial function genes. **(D)** Heatmaps depicting the correlation of pro-inflammatory (*Cd45*, *Il1*β, *Tnf-*α) and homeostatic (*Cx3cr1*, *P2ry12*, *Tgf*β*1*) microglial function genes with mitochondrial function genes as determined by linear regression analysis. See *Table S3* for R^2- and P-values. **(E)** Representative dot plots of FACS analyzed Saline, LPS 4hr, and LPS 24hr microglia comparing TMRM fluorescence intensity to GFP fluorescence intensity. **(F)** Quantification of Median Fluorescence Intensity of GFP, TMRM (individual cell TMRM signal was normalized to the same cell's GFP signal to account for mitochondrial mass), and CD45 signal in STR and MB microglia from Saline (N =7), LPS 4hr (N=7), and LPS 24hr (N = 7) mice. One-way ANOVA: GFP STR, $F_{(2,18)} = 25.06735$, $p < 0.0001$; GFP MB, $F_{(2,18)} = 29,85264$, $p < 0.0001$; TMRM STR, $F_{(2,18)} = 19.2316$, $p < 0.0001$; TMRM MB, $F_{(2,18)} = 6.61021$, $p = 0.00704$; CD45 STR, $F_{(2,18)} = 5.52274$, $p = 0.01348$; CD45 MB, $F_{(2,18)} = 2.99003$, $p = 0.07565$. * $P < 0.05$, t-test with Bonferroni correction.

FIGURE 5

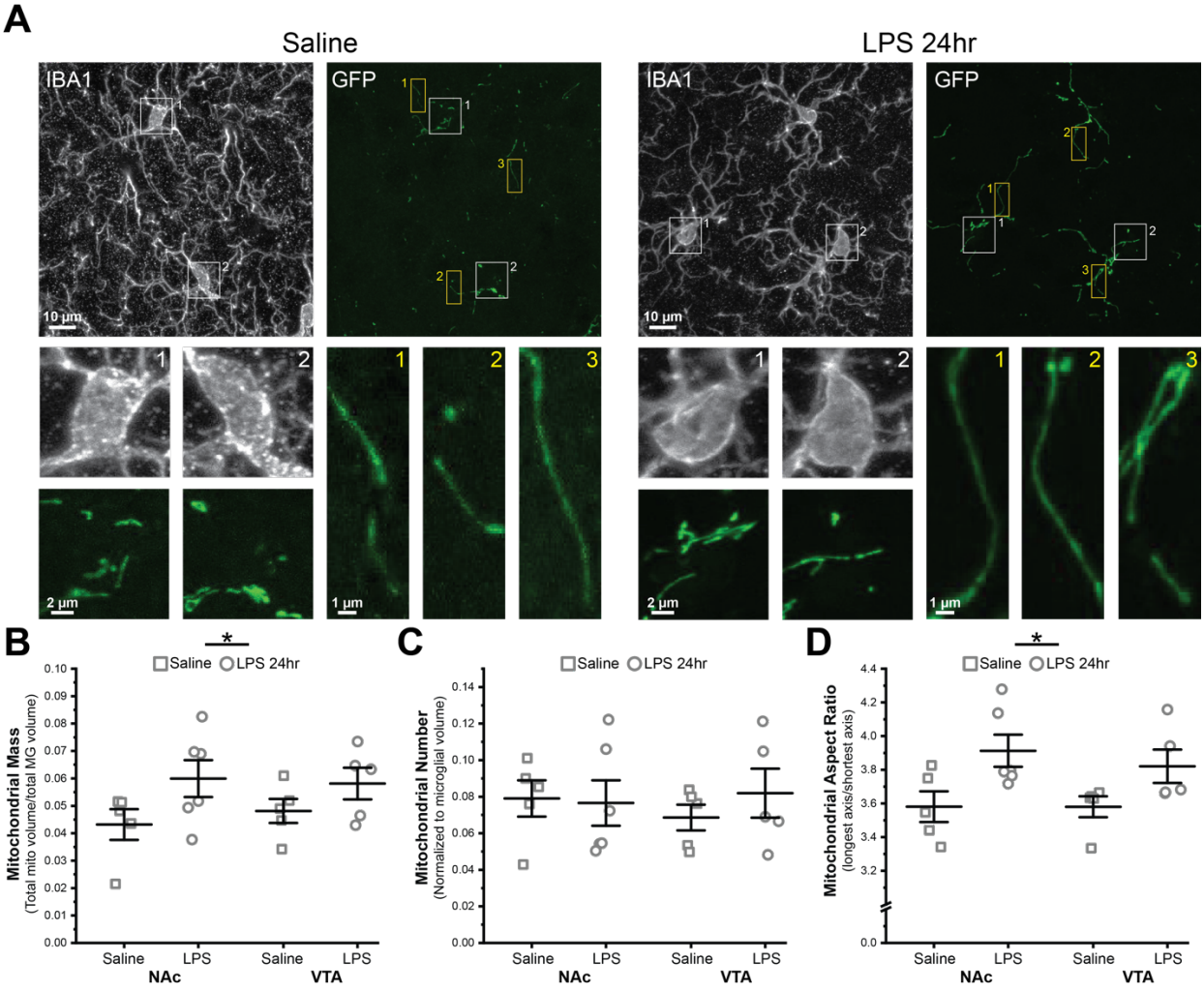

Figure 5: Microglial responses to inflammatory challenge (LPS) are accompanied by microglial elongation and increases mitochondrial mass. (A) Representative images of NAc microglia (IBA1) and their mitochondria (GFP) from 3-4mo *MG-MitoEGFP* mice injected with saline (*left*) or LPS 24hr (*right*). *White* and *yellow boxes* highlight microglial somas and cell processes where higher magnification zooms are shown *below*. **(B)** Quantification of microglial mitochondrial mass (mitochondrial volume / cell volume; Two-way ANOVA: main effect of treatment, $F_{(1,17)} = 5.19787$, p-value = 0.03579; main effect of region, $F_{(1,17)} = 0.0713$, p-value = 0.079266). **(C)** Quantification of mitochondrial number (relative to cell volume; Two-way ANOVA: main effect of treatment, $F_{(1,17)} = .23167$, p-value = 0.63642; main effect of region, $F_{(1,17)} = 0.05079$, p-

value = 0.82438). **(D)** Quantification of mitochondrial aspect ratio (longest axis / shortest axis; Two-way ANOVA: main effect of treatment, $F_{(1,17)} = 10.19319$, p-value = 0.00533; main effect of region, $F_{(1,17)} = 0.26571$, p-value = 0.61286). N = 5-6 mice per group.

FIGURE 6

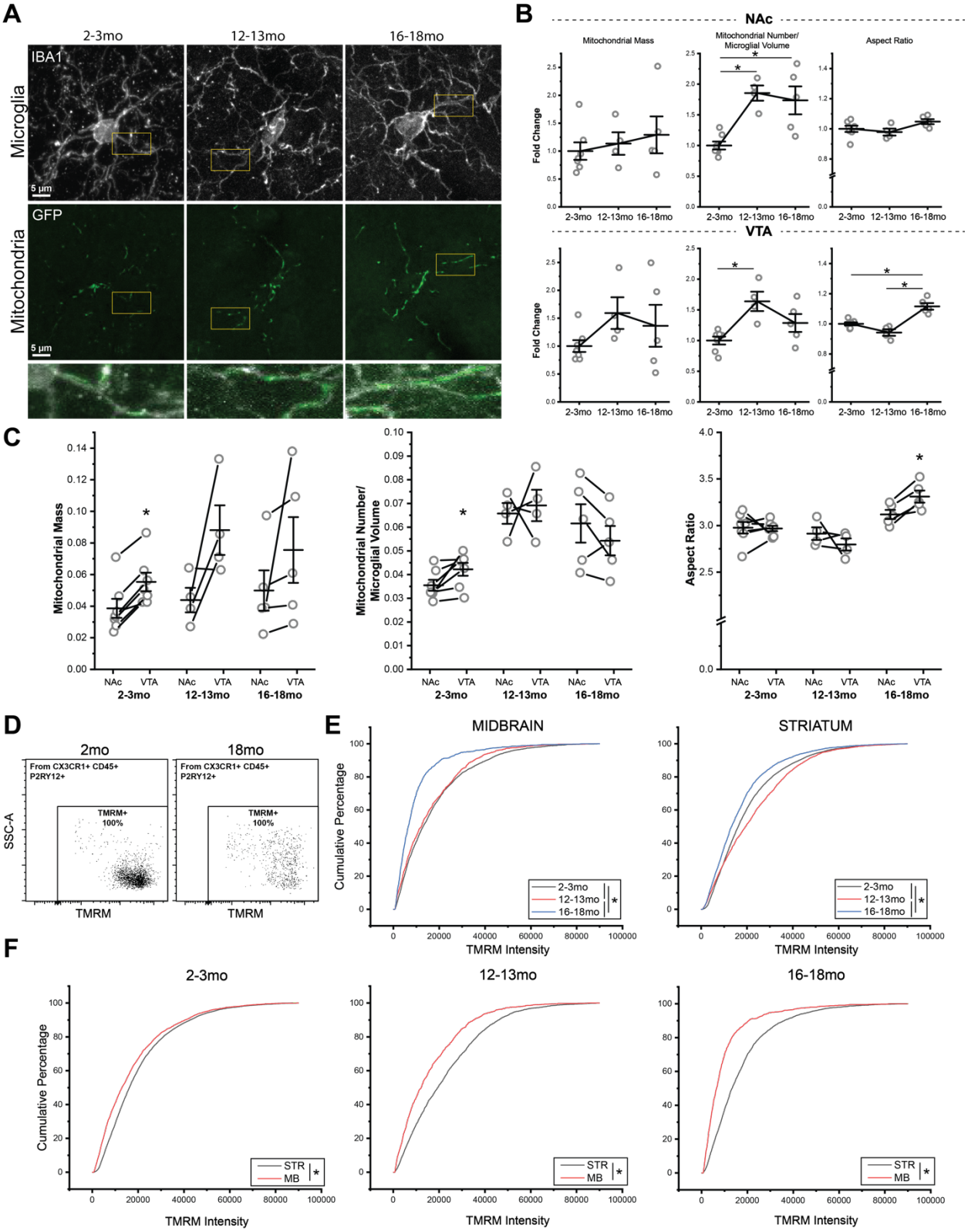
A
2-3mo
12-13mo
16-18mo
Microglia
IBA1
5 µm
Mitochondria
GFP
5 µm
B
NAc
Mitochondrial Mass
Mitochondrial Number/ Microglial Volume
Aspect Ratio
Fold Change
2-3mo 12-13mo 16-18mo
VTA
C
Mitochondrial Mass
Mitochondrial Number/ Microglial Volume
Aspect Ratio
NAc VTA
2-3mo
12-13mo
16-18mo
D
2mo
18mo
From CX3CR1+ CD45+ P2RY12+
TMRM+ 100%
SSC-A
TMRM
E
MIDBRAIN
STRIATUM
Cumulative Percentage
TMRM Intensity
2-3mo
12-13mo
16-18mo
F
2-3mo
12-13mo
16-18mo
STR
MB
Cumulative Percentage
TMRM Intensity

Figure 6: Microglial mitochondria undergo remodeling in middle- and late middle age. (A) Representative images of NAc microglia (IBA1) and microglial mitochondria (GFP) from 2-3mo, 12-13mo, and 16-18mo *MG-MitoEGFP* mice. **(B)** Mitochondrial mass, number, and aspect ratio of NAc and VTA microglia during aging, normalized to mean values from 2-3mo animals. One-Way ANOVA: NAc Mitochondrial Mass, $F_{(2,13)} = 0.43588$, $p = 0.65581$; VTA Mitochondrial Mass, $F_{(2,13)} = 1.47803$, $p = 0.26401$; NAc Mitochondrial Number, $F_{(2,13)} = 11.5342$, $p = 0.00132$; VTA Mitochondrial Number, $F_{(2,13)} = 7.57294$, $p = 0.0066$; NAc Mitochondrial Aspect Ratio, $F_{(2,13)} = 2.54264$, $p = 0.11695$; VTA Mitochondrial Aspect Ratio, $F_{(2,13)} = 24.40763$, $p < 0.0001$. * $P < 0.05$, two sample t-test with Bonferonni correction. **(C)** Comparison of NAc and VTA microglial mitochondria from individual 2-3mo, 12-13mo, and 16-18mo mice. * $p< 0.05$, two tailed, paired t-test. **(D)** Representative dot plots from FACS analysis of 2-3mo and 16-18mo WT microglia showing TMRM fluorescence intensity (measure of mitochondrial membrane potential) and side scatter (SSC, measure of internal cell complexity). **(E)** Cumulative probability distribution of TMRM fluorescence intensity of midbrain microglia (*left*) and striatum microglia (*right*) from 2-3mo, 12-13mo, and 16-18mo mice. Kolmogorov-Smirnov tests comparing ages within each region show that distributions at each age are significantly different from one another. * $P < 0.05$. **(F)** Cumulative probability distribution of TMRM fluorescence intensity comparing midbrain and striatum microglia at each age. Kolmogorov-Smirnov tests show that midbrain and striatum distributions at each age are significantly different from one another. * $P < 0.05$.

SUPPLEMENTARY FIGURE 1

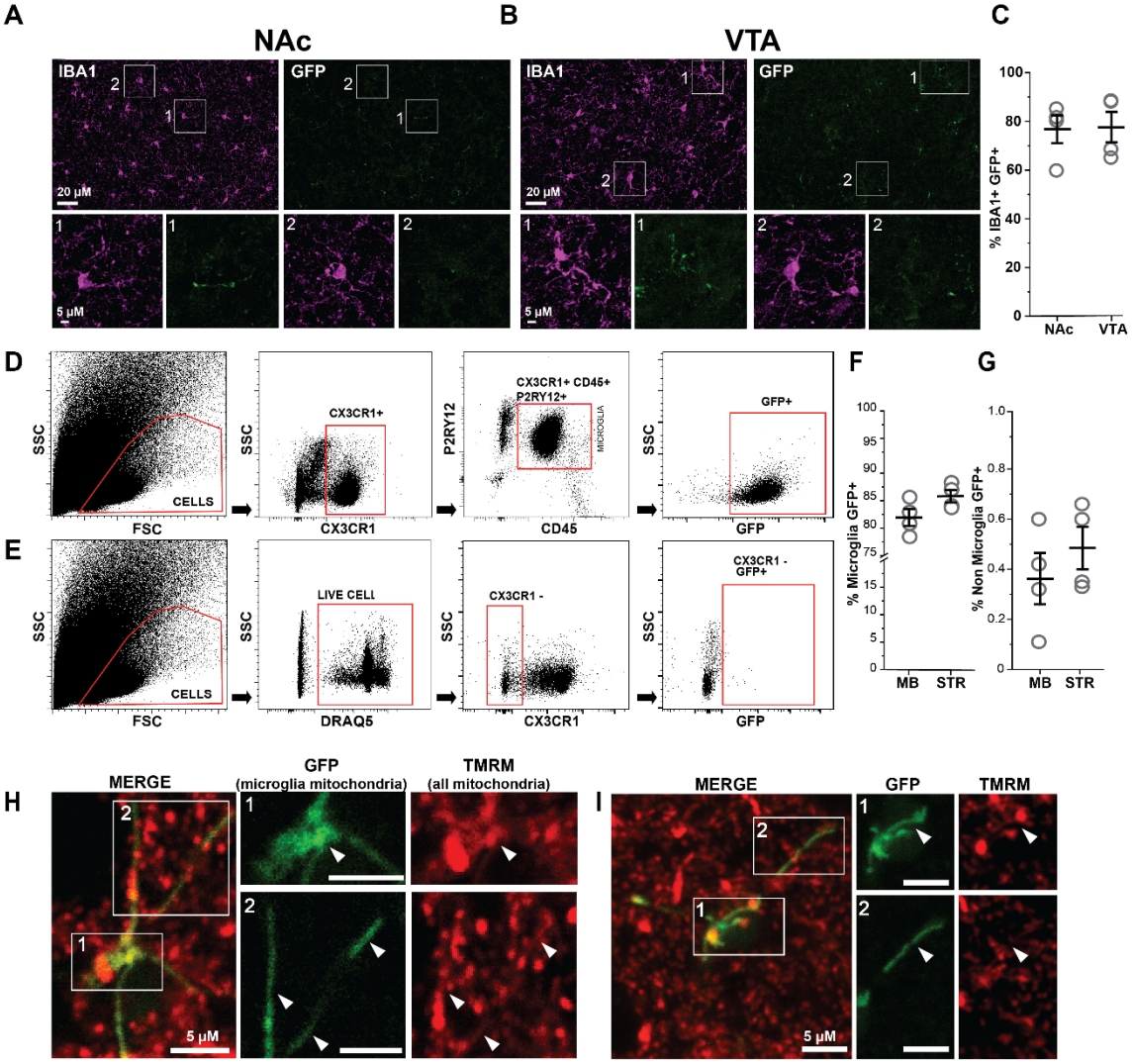

FIGURE S1: Validation of *CX3CR1-CreER; flox-stop mitoEGFP* (*MG-MitoEGFP*) mice. (A) 20x confocal images of native EGFP signal and Iba1 (magenta) staining in *CX3CR1-CreER; flox-stop mitoEGFP* (*MG-MitoEGFP*) mice showing that all EGFP labeled mitochondria are within Iba1+. Box 1 and 2 examples of IBA1+ GFP+ positive cells and IBA1+GFP- cells. **(B)** Showing native EGFP signal in VTA. **(C)** Quantification of percentage of microglia showing recombination and expression of EGFP in mitochondria in nucleus accumbens (NAc) and ventral tegmental area (VTA). **(D)** FACS-based analysis in midbrain (MB) and striatum (STR) of percentage of microglia showing recombination. Sequential gating strategy shown, CX3CR1+P2RY12+CD45+ putative microglia isolated and GFP+ gate shown. **(E)** Gating strategy for live cells

(DRAQ5+), non-microglia (CX3CR1-) and GFP+ shown. **(F-G)** Percentage of microglia (CX3CR1+P2RY12+CD45+) and non-microglial cells (CX3CR1- Draq5+) showing expression of GFP in MB and STR. **(H-I)** Live imaging of acute brain sections from *MG-MitoEGFP* mice incubated with mitochondrial membrane potential indicator dye TMRM. Examples 1 and 2 show co-labeling of GFP and TMRM. Zoom 1 shows cell body colocalization and zoom 2 shows colocalization in the processes.

SUPPLEMENTARY FIGURE 2

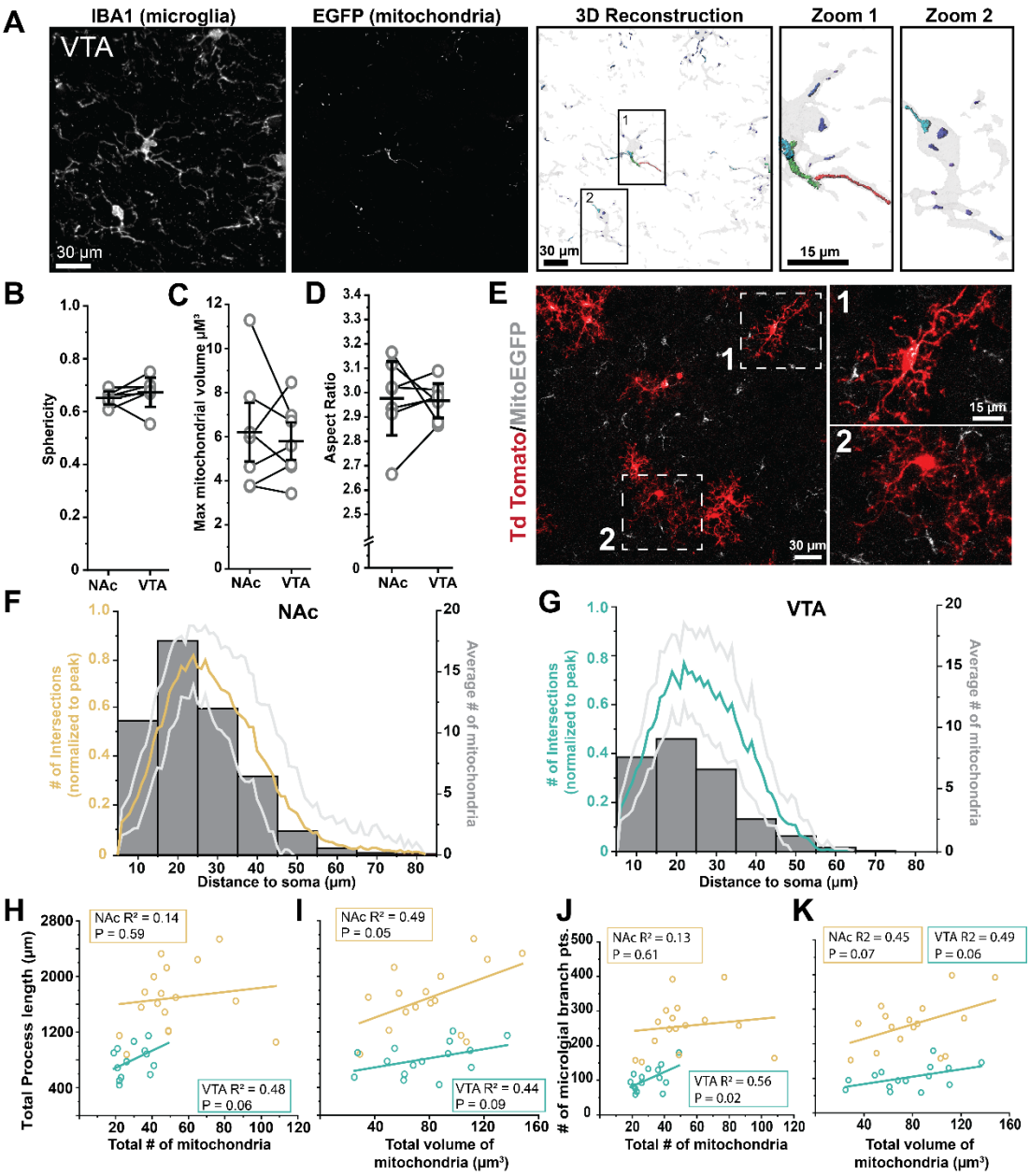

FIGURE S2: Mitochondrial morphology network changes are heterogeneous in microglia (continuation Fig.1) (A) Representative high-magnification images at P60 of NAc microglia (Iba1) and mitochondria (EGFP); 3D reconstructions of mitochondria (colored according to volume) and zoomed in panels (1 and 2) on bottom left depicting colocalized surfaces. **(B-D)** Quantification of mitochondrial parameters at P60 across regions (NAc, VTA). Within a given age, data points that come from the same mouse

are identified by the connecting line. *B-D*. NAc vs VTA P60 p=0.346, n.s paired t-test for sphericity and p=0.640, n.s for max mitochondria volume normalized to microglial volume, paired t-test p=0.894 aspect ratio = long axis divided by short axis. **(E)** Representative 20x image of TdTom and mitoEGFP sparse labeling. **(F-G)** Sholl analysis of individual reconstructed microglia; normalized to peak and averaged across regions (NAc N=16 and VTA N=15). **(H-K)** Linear regression plots for showing relationships between microglial process length and mitochondrial morphological parameters for both regions (NAc N=16 and VTA N=15). *H-I.* linear regression NAc R2 = 0.49 p=0.05 for total process length vs total volume of mitochondria, NAc R2 = 0.14 p=0.59 VTA R2 = 0.48 p=0.06 for total process length vs total number of mitochondria. *J-K.* NAc R2 = 0.13 p=0.61 VTA=0.56 p=0.02 for number of mg branch pts vs total number of mitochondria, *K.* NAc R2 = 0.45 p=0.07 VTA R2 = 0.49 p=0.06 for number of mg branch pts vs total volume of mitochondria.

SUPPLEMENTARY FIGURE 3

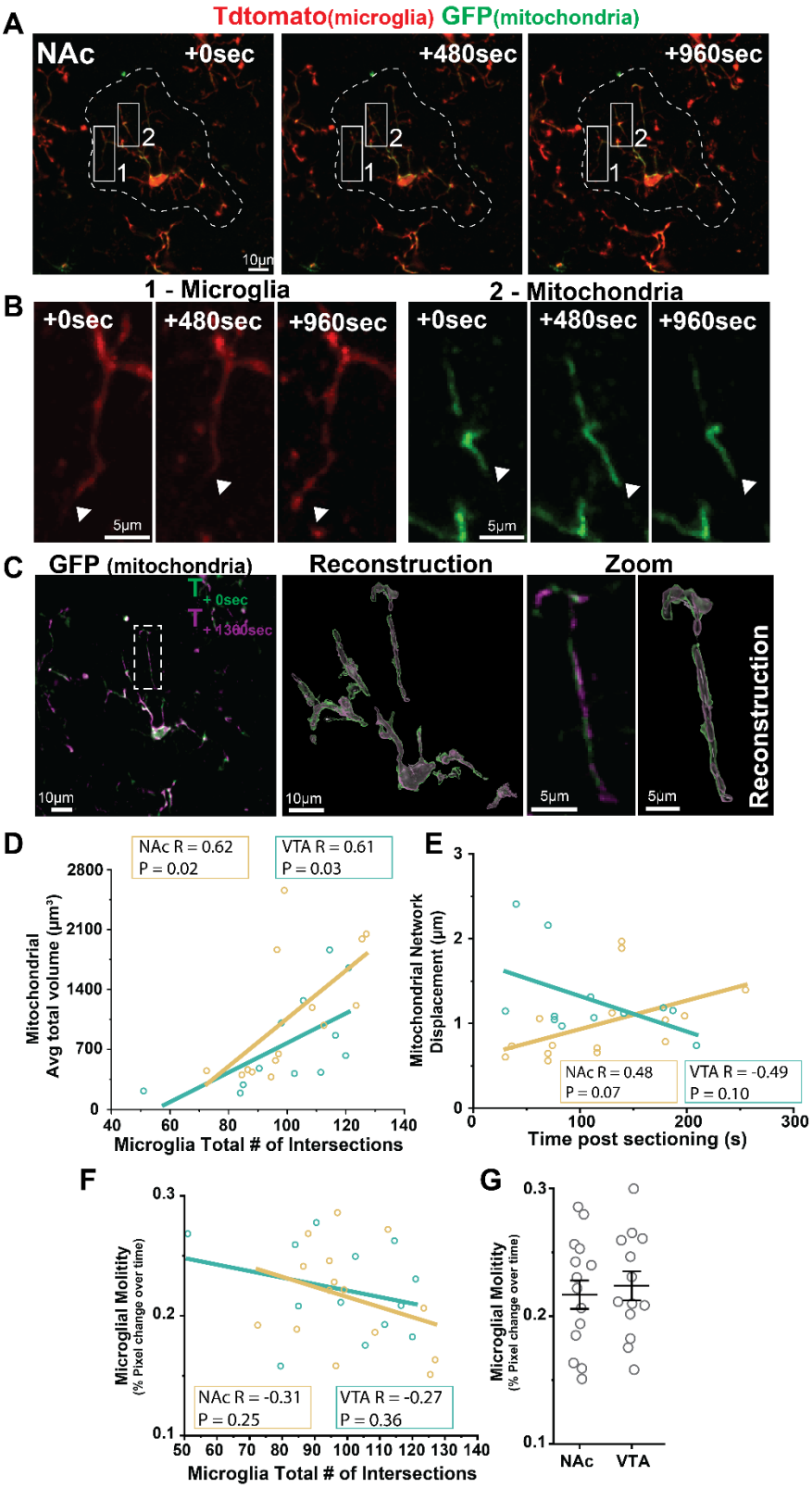

FIGURE S3: Microglial mitochondria present dynamic motility and network remodeling. (related to Fig.2). (A) Representative images of first frame and last frame of acute brain slice of NAc microglia (Td Tomato) and mitochondria (EGFP) at 1.5-2mos old mice. **(B)** Example of microglia process retraction/extension and mitochondrial displacement indicated by white arrow at different timepoints. **(C)** 3D reconstructions of mitochondria (colored by time frame) and zoomed in panels on right depicting fluorescence and respective surface reconstruction. **(D)** Linear regression plots for showing relationships between mitochondrial avg. total volume and microglial number of inters. NAc R2 = 0.62 p=0.02, VTA R2 = 0.61 p=0.03. **(E)** Linear regression plots of mitochondrial network displacement and time post sectioning. *E.* NAc R2 = -0.48 p=0.07 VTA R2 = -0.49 p=0.10. **(F)** Linear regression analysis of microglial motility and microglial total number of intersections (ImageJ sholl analysis). *E*. NAc R2 = -0.31 p=0.25 VTA R2 = -0.27 p=0.36 for microglial motility vs microglial total number of inters. **(G)** Quantification of microglial motility in both NAc and VTA.

SUPPLEMENTARY FIGURE 4

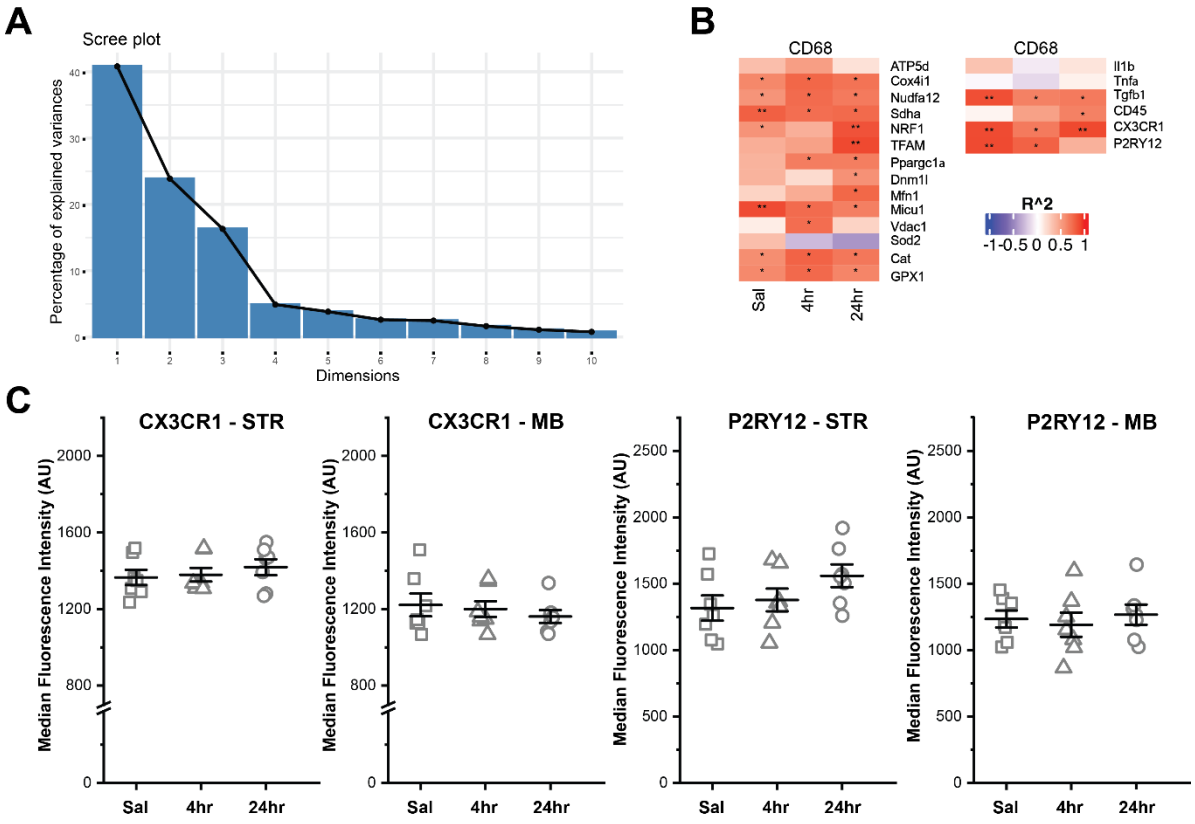

Figure S4: Microglial and mitochondrial responses to inflammatory challenge (LPS) (related to Fig. 4). (A) Scree plot describing the percentage of explained variance for the Principal Component Analysis of saline, LPS 4hr, and LPS 24hr samples based only on mitochondrial function genes. **(B)** Heat maps depicting the correlation of Cd68 with microglial function genes and mitochondrial function genes as analyzed by linear regression. See Supp Table 4 for R2- and P-values. **(C)** Quantification of Median Fluorescent Intensity of CX3CR1 and P2RY12 signal in the STR and MB of Saline (N =7), LPS 4hr (N=7), and LPS 24hr (N = 7) samples. Samples are not significantly different by treatment but were significantly different by region. Two-way ANOVA: CX3CR1 Treatment, $F(2,36) = 0.00442$, $p = 0.99559$, Region, $F(1,36) = 30.80804$, $p < 0.0001$; P2RY12 Treatment, $F(2,36) = 1.71502$, $p = 0.19514$, Region $F(1,36) = 7.52567$, $p = 0.00942$.

SUPPLEMENTARY FIGURE 5

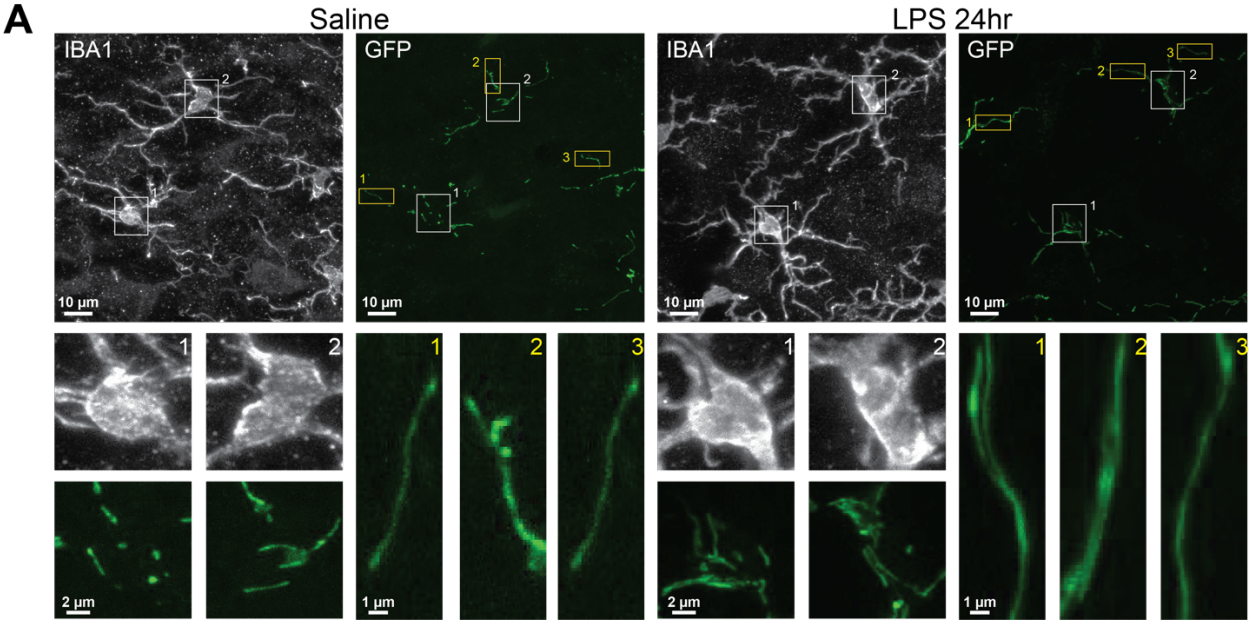

Figure S5: VTA microglial mitochondrial response to inflammatory challenge (LPS) (related to Fig. 5). **(A)** Representative images of VTA microglia (IBA1) and microglial mitochondria (GFP) of 3-4mo *MG-MitoEGFP* mice injected with saline (left) or LPS 24hr (right) prior to euthanasia. Zoomed panels depict example somatic mitochondria (white frame) and cell process mitochondria (yellow frame).

SUPPLEMENTARY FIGURE 6

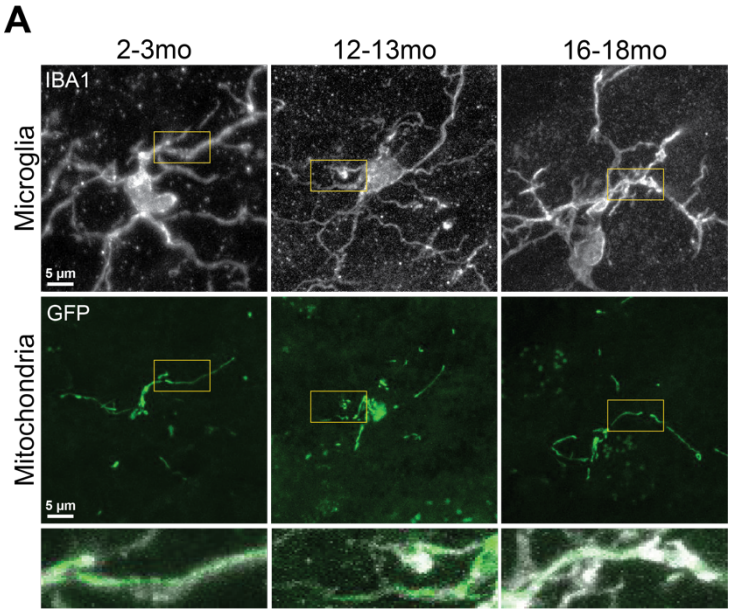

Figure S6: VTA microglial mitochondria undergo remodeling in middle- and late middle age (related to Fig. 6). (A) Representative images of VTA microglia (IBA1) and microglial mitochondria (GFP) from 2-3mo, 12-13mo, and 16-18mo *MG-MitoEGFP* mice.

Supplementary Table 1: LPS Relative Gene Expression ANOVA Values.
Related to Figure 4B.

	Treatment		Region	
Gene	F Value	P Value	F Value	P Value
Tgfβ1	3.64818	0.03638	0.74976	0.39245
P2ry12	13.3998	0.0001	0.68065	0.41495
Csf1r	1.13966	0.34319	1.2454	0.27996
Cx3cr1	9.42003	0.000533	0.04288	0.83715
Cd68	4.11485	0.02483	5.06765	0.03076
Cd45	8.86009	0.00077	7.37401	0.01021
Itgam	14.09506	0.000246	1.07928	0.31341
Tnfα	10.23143	0.000317	0.01671	0.8979
Il1β	8.41188	0.00104	0.01627	0.89925
Micu1	5.40554	0.009	5.57555	0.02391
Cat	7.43629	0.00204	0.11711	0.73424
Ppargc1α	2.99706	0.06289	0.15601	0.69526
Nrf1	4.43215	0.01924	0.04594	0.83152
Mfn1	0.77771	0.46724	1.3191	0.25854
Dnm1l	4.8918	0.01338	0.31082	0.58072
Sod2	7.41671	0.00206	1.70341	0.20036
Tfam	2.1335	0.13357	1.72655	0.1974
Vdac1	12.4427	0.0001	0.06818	0.79554
Gpx1	20.79043	0.0001	1.01441	0.32076
Ndufa12	15.1893	0.0001	0.31724	0.57686
Atp5d	36.99749	0.0001	2.90216	0.09733
Cox4i1	12.11631	0.0001	1.69829	0.20102
Sdha	1.8012	0.18007	0.00647	0.93633

Supplementary Table 2: LPS Relative Gene Expression Post Hoc Analyses.
Related to Figure 4B.

Genes		LPS 4hr vs Saline	LPS 24hr vs Saline	LPS 24hr vs LPS 4hr	MB vs STR
Tgfβ1	Probability	0.29856	0.03572	1	0.41278
	T value	-1.69206	-2.65327	-0.91161	-0.8289
P2ry12	Probability	0.00101	0.0001	1	0.45099
	T value	-3.97331	-4.8306	-0.76698	-0.76229
Csf1r	Probability	0.56513	1	1	0.33355
	T value	-1.37044	-0.94236	0.46004	-0.99552
Cx3cr1	Probability	0.00041798	0.45199	0.02272	0.95445
	T value	-4.27642	-1.46937	2.83451	-0.05753
Cd68	Probability	0.17688	1	0.03203	0.03952
	T value	-1.95212	0.75952	2.69744	-2.13869
Cd45	Probability	1	0.00219	0.00309	0.00733
	T value	0.05282	3.7024	3.58036	2.84717
Itgam	Probability	0.2025	0.000191597	0.01835	0.25439
	T value	1.95288	5.25978	3.12856	1.17964
Tnfα	Probability	0.000198161	0.117796	0.03916	0.9941
	T value	4.52848	1.9492	-2.61572	-0.00745
Il1β	Probability	0.00078693	0.42024	0.04286	0.98861
	T value	4.06006	1.50976	-2.57852	-0.01438
Micu1	Probability	0.27588	0.00708	0.4393	0.02479
	T value	-1.73266	-3.27919	-1.48524	-2.34559
Cat	Probability	0.00198	0.04203	0.71437	0.82245
	T value	-3.73851	-2.58666	1.2002	-0.22609
Ppargc1α	Probability	0.16869	0.09614	1	0.71262
	T value	-1.97473	-2.23293	-0.21646	-0.37134
Nrf1	Probability	0.21664	0.78056	0.01577	0.89431
	T value	1.85378	-1.24449	-2.97688	0.13382
Mfn1	Probability	1	0.76394	1	0.23403
	T value	-0.95289	-1.15815	-0.18361	1.21095
Dnm1l	Probability	0.02817	0.03151	1	0.58201
	T value	2.7491	2.70405	-0.0956	0.55561
Sod2	Probability	0.02418	0.00246	1	0.21081
	T value	2.80989	3.6624	0.78404	1.2747
Tfam	Probability	0.14411	0.35257	1	0.20397
	T value	2.04883	1.6048	-0.47402	-1.2945
Vdac1	Probability	0.09993	0.027	0.0001	0.64942
	T value	-2.2157	2.76603	4.93002	0.4585
Gpx1	Probability	0.06221	0.000865327	0.0001	0.2331
	T value	-2.42235	4.02733	6.3744	1.2134
Nudfa12	Probability	1	0.0001	0.00026155	0.66075
	T value	0.4567	4.98498	4.43509	-0.44264
Atp5d	Probability	1	0.0001	0.0001	0.13839
	T value	-0.26036	7.3228	7.44627	-1.51645
Cox4i1	Probability	1	0.000437904	0.00068819	0.25917
	T value	0.065	4.26059	4.11594	-1.14698
Sdha	Probability	0.32009	1	0.38157	0.98235
	T value	-1.65582	-0.0952	1.5624	0.02229

Supplementary Table 3: LPS Microglila- and Mitochondrial- Function Gene Correlation Values. Related to Figure 4D.

		Cd45			Il1β			Tnfα		
Genes		Saline	LPS 4hr	LPS 24hr	Saline	LPS 4hr	LPS 24hr	Saline	LPS 4hr	LPS 24hr
Atp5d	p-value	0.243186	0.054409	0.422675	0.655035	0.261958	0.068148	0.453851	0.737764	0.07301
	R value	0.334	0.524	0.233	0.131	0.322	0.501	0.218	0.098	0.493
Cox4i1	p-value	0.115781	0.020008	0.008949	0.162115	0.343098	0.155616	0.112976	0.857977	0.295356
	R value	0.44	0.612	0.669	0.395	0.274	0.401	0.443	-0.053	0.301
Nudfa12	p-value	0.242291	0.00231	0.001688	0.718613	0.041942	0.050471	0.649297	0.147684	0.020906
	R value	0.335	0.743	0.758	0.106	0.549	0.531	0.133	0.408	0.609
Sdha	p-value	0.450617	0.000284	0.00158	0.658862	0.074233	0.875813	0.958116	0.301592	0.846165
	R value	0.22	0.825	0.761	0.13	0.492	0.046	0.015	0.298	0.057
Nrf1	p-value	0.259407	0.000842	0.003925	0.852717	0.008988	0.760069	0.69175	0.00567	0.832857
	R value	0.323	0.787	0.717	0.055	0.668	-0.09	0.116	0.696	-0.062
Tfam	p-value	0.874163	0.004251	0.006326	0.803208	0.005939	0.421008	0.499075	0.014526	0.603661
	R value	0.047	0.712	0.69	-0.073	0.694	0.234	-0.197	0.636	0.152
Ppargc1α	p-value	0.518132	0.007551	0.125748	0.219981	0.5074	0.309656	0.239796	0.563102	0.475501
	R value	-0.189	0.679	0.429	-0.35	0.194	0.293	-0.336	0.169	0.208
Dnm1l	p-value	0.255455	0.027207	1.86E-05	0.903408	0.001987	0.103279	0.573546	0.000308	0.023148
	R value	0.326	0.587	0.891	-0.036	0.75	0.454	0.165	0.822	0.601
Mfn1	p-value	0.298008	0.000239	0.000604	0.46486	0.006849	0.667476	0.703702	0.039963	0.565706
	R value	0.3	0.83	0.799	-0.213	0.685	0.126	0.112	0.554	0.168
Micu1	p-value	0.637384	0.006495	0.200337	0.183293	0.099527	0.223598	0.829954	0.623895	0.110662
	R value	0.138	0.688	0.364	0.378	0.458	-0.347	0.063	0.144	-0.445
Vdac1	p-value	0.132387	0.006258	0.026315	0.768373	0.722023	0.17943	0.202406	0.408627	0.236248
	R value	0.422	0.691	0.59	0.087	0.105	0.381	0.363	-0.24	0.339
Sod2	p-value	0.095783	0.656759	0.791282	0.332263	0.00051	0.049946	0.093852	0.00047	0.008993
	R value	0.463	0.13	0.078	0.28	0.805	0.533	0.465	0.808	0.668
Cat	p-value	0.017759	0.068415	0.15402	0.112545	0.31547	0.273258	0.074569	0.050841	0.146902
	R value	0.621	0.5	0.402	0.443	-0.289	-0.315	0.491	-0.531	-0.409
Gpx1	p-value	0.040339	0.116319	0.000114	0.070438	0.147068	0.307691	0.290397	0.104706	0.180963
	R value	0.553	0.439	0.851	0.497	-0.408	0.294	0.304	-0.452	0.379

		Cx3cr1			P2ry12			Tgfβ1		
Genes		Saline	LPS 4hr	LPS 24hr	Saline	LPS 4hr	LPS 24hr	Saline	LPS 4hr	LPS 24hr
Atp5d	p-value	0.410507	0.507675	0.934088	0.476733	0.513171	0.115752	0.18298	0.017449	0.43138
	R value	0.239	0.193	0.024	0.207	0.191	-0.44	0.378	0.622	-0.229
Cox4i1	p-value	0.002718	0.059727	0.001538	0.04562	0.047682	0.564532	0.000121	0.01133	0.129875
	R value	0.736	0.515	0.762	0.541	0.537	0.169	0.849	0.653	0.425
Nudfa12	p-value	0.008378	0.623349	0.076011	0.006493	0.366739	0.371298	0.006554	0.002106	0.869059
	R value	0.673	0.144	0.489	0.688	0.261	-0.259	0.688	0.748	0.049
Sdha	p-value	0.004549	0.382336	0.000201	0.000489	0.250465	0.06339	0.005378	0.010413	0.00232
	R value	0.709	0.253	0.835	0.807	0.329	0.508	0.699	0.659	0.743
Nrf1	p-value	0.026509	0.616306	7.19E-05	0.00873	0.816145	0.046178	0.011859	0.021657	0.008035
	R value	0.59	-0.147	0.863	0.67	-0.068	0.54	0.65	0.606	0.675
Tfam	p-value	0.156288	0.530575	2.73E-06	0.018423	0.767284	0.103588	0.133879	0.013729	0.007085
	R value	0.4	-0.183	0.922	0.618	-0.087	0.453	0.421	0.64	0.683
Ppargc1α	p-value	0.305367	0.331094	0.031964	0.037368	0.171057	0.151528	0.376428	0.048401	0.054397
	R value	0.295	0.281	0.574	0.56	0.387	0.404	0.256	0.536	0.524
Dnm1l	p-value	0.115107	0.075744	0.035223	0.129566	0.169954	0.666568	0.16688	0.09772	0.664119
	R value	0.44	-0.489	0.565	0.425	-0.388	-0.126	0.391	0.46	0.127
Mfn1	p-value	0.246613	0.779622	6.76E-05	0.26496	0.973076	0.093375	0.374466	0.025203	0.012711
	R value	0.332	-0.082	0.864	0.32	-0.01	0.466	0.257	0.594	0.645
Micu1	p-value	0.006706	0.152296	0.000361	0.002054	0.093731	4.12E-05	0.002998	0.00414	9.65E-05
	R value	0.686	0.404	0.817	0.749	0.465	0.875	0.731	0.714	0.855
Vdac1	p-value	0.818976	0.020545	0.137403	0.975162	0.021355	0.85242	0.427631	0.044513	0.503071
	R value	0.067	0.61	0.418	0.009	0.607	0.055	0.231	0.544	0.195
Sod2	p-value	0.228609	0.030824	0.139799	0.410051	0.049988	0.029747	0.047076	0.216666	0.057862
	R value	0.344	-0.577	-0.415	0.239	-0.532	-0.58	0.538	0.352	-0.518
Cat	p-value	0.026453	8.66E-07	5.16E-05	0.084368	1.86E-06	8.73E-06	0.002832	0.078165	2.00E-06
	R value	0.59	0.936	0.87	0.477	0.927	0.905	0.733	0.486	0.926
Gpx1	p-value	0.002105	0.000371	0.006925	0.04628	0.00011	0.995596	0.00704	0.157777	0.272069
	R value	0.748	0.816	0.684	0.54	0.852	-0.002	0.683	0.399	0.315

Supplementary Table 4: LPS CD68 and Mitochondrial Function Gene Correlation Values. Related to Figure S4.

		Cd68		
Genes		Saline	LPS 4hr	LPS 24hr
Atp5d	p-value	0.244953	0.072956	0.597781
	R value	0.333	0.493	0.155
Cox4i1	p-value	0.022299	0.001642	0.005179
	R value	0.604	0.759	0.701
Nudfa12	p-value	0.044364	0.002696	0.009273
	R value	0.544	0.736	0.666
Sdha	p-value	0.000925	0.003644	0.002434
	R value	0.783	0.721	0.741
Nrf1	p-value	0.041921	0.147633	0.000147
	R value	0.549	0.408	0.844
Tfam	p-value	0.142168	0.082639	2.80E-05
	R value	0.413	0.48	0.883
Ppargc1α	p-value	0.168117	0.011502	0.01246
	R value	0.39	0.652	0.647
Dnm1l	p-value	0.16642	0.521566	0.038072
	R value	0.391	0.187	0.558
Mfn1	p-value	0.426371	0.12996	0.001682
	R value	0.231	0.425	0.758
Micu1	p-value	4.48E-05	0.002633	0.013571
	R value	0.873	0.737	0.641
Vdac1	p-value	0.717459	0.003202	0.437407
	R value	0.106	0.727	0.226
Sod2	p-value	0.245894	0.313307	0.101732
	R value	0.332	-0.291	-0.455
Cat	p-value	0.031319	0.001214	0.007711
	R value	0.575	0.772	0.678
Gpx1	p-value	0.023396	0.002231	0.017928
	R value	0.6	0.745	0.62
Il1β	p-value	0.285311	0.743132	0.633467
	R value	0.307	-0.096	0.14
Tnfα	p-value	0.890133	0.573917	0.779166
	R value	-0.041	-0.165	0.083
Tgfβ1	p-value	8.64E-05	0.01461	0.009268
	R value	0.858	0.635	0.666
Cd45	p-value	0.814098	0.083225	0.01459
	R value	0.069	0.479	0.635
Cx3cr1	p-value	4.05E-05	0.009317	2.61E-05
	R value	0.876	0.666	0.885
P2ry12	p-value	3.48E-05	0.001087	0.157866
	R value	0.879	0.777	0.399

Supplementary Table 5: Primers and probes used for qPCR experiments. Related to Figures 4 and S4.

Gene	TaqMan Assay ID or custom probe	Forward Primer	Reverse Primer
Aldh1l1	Mm03048957_m1		
Atp5d	Mm00502864_m1		
Cat	Mm00437992_m1		
Cd45 (Ptprc)	Mm01293577_m1		
Cd68	Mm03047343_m1		
Cox4i1	Mm01250094_m1		
Csrf1	Mm01266652_m1		
Cx3cr1	Mm00438354_m1		
Dnm1l	Mm01342903_m1		
Gapdh	MGB - CTCATGACCACAGTCCA - VIC	GACAACTTTGGCATTGTGGAA	CACAGTCTTCTGGGTGGCAGTGA
Gpx1	Mm04207457_g1		
Il1β	Mm00434228_m1		
Itgam	Mm00434455_m1		
Mfn1	Mm00612599_m1		
Micu1	Mm00522783_m1		
Nrf1	Mm01135606_m1		
Nudfa12	Mm01240336_m1		
Olig1	Mm00497537_s1		
Olig2	Mm01210556_m1		
P2ry12	Mm00446026_m1		
Ppargc1α	Mm01208835_m1		
Ppp1r1b	Mm00454892_m1		
Sdha	Mm01352366_m1		
Slc1a2	Mm01275814_m1		
Slc32a1	Mm00494138_m1		
Sod2	Mm01313000_m1		
Tfam	Mm01148667_m1		
Tgfβ1	Mm01178820_m1		
Tnfα	Mm00443258_m1		
Vdac1	Mm00834272_m1		

REFERENCES

1. Li Q, Barres BA. Microglia and macrophages in brain homeostasis and disease. Nat Rev Immunol. 2018 Apr;18(4):225–42.

2. Sierra A, Paolicelli RC, Kettenmann H. Cien Años de Microglía: Milestones in a Century of Microglial Research. Trends Neurosci. 2019 Nov;42(11):778–92.

3. Matsudaira T, Prinz M. Life and death of microglia: Mechanisms governing microglial states and fates. Immunol Lett. 2022 May;245:51–60.

4. Silvin A, Qian J, Ginhoux F. Brain macrophage development, diversity and dysregulation in health and disease. Cell Mol Immunol. 2023 Nov;20(11):1277–89.

5. Thion MS, Garel S. On place and time: microglia in embryonic and perinatal brain development. Curr Opin Neurobiol. 2017 Dec;47:121–30.

6. Frost JL, Schafer DP. Microglia: Architects of the Developing Nervous System. Trends Cell Biol. 2016 Aug;26(8):587–97.

7. Hammond TR, Dufort C, Dissing-Olesen L, Giera S, Young A, Wysoker A, et al. Single-Cell RNA Sequencing of Microglia throughout the Mouse Lifespan and in the Injured Brain Reveals Complex Cell-State Changes. Immunity. 2019 Jan 15;50(1):253-271.e6.

8. Bennett ML, Bennett FC, Liddelow SA, Ajami B, Zamanian JL, Fernhoff NB, et al. New tools for studying microglia in the mouse and human CNS. Proc Natl Acad Sci U S A. 2016 Mar 22;113(12):E1738–46.

9. Matcovitch-Natan O, Winter DR, Giladi A, Vargas Aguilar S, Spinrad A, Sarrazin S, et al. Microglia development follows a stepwise program to regulate brain homeostasis. Science. 2016 Aug 19;353(6301):aad8670.

10. Grabert K, Michoel T, Karavolos MH, Clohisey S, Baillie JK, Stevens MP, et al. Microglial brain region−dependent diversity and selective regional sensitivities to aging. Nat Neurosci. 2016 Mar;19(3):504–16.

11. Stowell RD, Wong EL, Batchelor HN, Mendes MS, Lamantia CE, Whitelaw BS, et al. Cerebellar microglia are dynamically unique and survey Purkinje neurons in vivo. Developmental Neurobiology. 2018;78(6):627–44.

12. Paolicelli RC, Sierra A, Stevens B, Tremblay ME, Aguzzi A, Ajami B, et al. Microglia states and nomenclature: A field at its crossroads. Neuron. 2022 Nov 2;110(21):3458–83.

13. Böttcher C, Schlickeiser S, Sneeboer MAM, Kunkel D, Knop A, Paza E, et al. Human microglia regional heterogeneity and phenotypes determined by multiplexed single-cell mass cytometry. Nat Neurosci. 2019 Jan;22(1):78–90.

14. De Biase LM, Bonci A. Region-Specific Phenotypes of Microglia: The Role of Local Regulatory Cues. Neuroscientist. 2019 Aug 1;25(4):314–33.

15. Ayata P, Badimon A, Strasburger HJ, Duff MK, Montgomery SE, Loh YHE, et al. Epigenetic regulation of brain region-specific microglia clearance activity. Nat Neurosci. 2018 Aug;21(8):1049–60.

16. Hanamsagar R, Bilbo SD. Environment matters: microglia function and dysfunction in a changing world. Curr Opin Neurobiol. 2017 Dec;47:146–55.

17. Salter MW, Stevens B. Microglia emerge as central players in brain disease. Nat Med. 2017 Sep 8;23(9):1018–27.

18. Wolf SA, Boddeke HWGM, Kettenmann H. Microglia in Physiology and Disease. Annu Rev Physiol. 2017 Feb 10;79:619–43.

19. Gleichman AJ, Carmichael ST. Glia in neurodegeneration: Drivers of disease or along for the ride? Neurobiol Dis. 2020 Aug;142:104957.

20. Ceasrine AM, Bilbo SD. Dietary fat: a potent microglial influencer. Trends Endocrinol Metab. 2022 Mar;33(3):196–205.

21. Sequeira MK, Bolton JL. Stressed Microglia: Neuroendocrine-Neuroimmune Interactions in the Stress Response. Endocrinology. 2023 Jun 6;164(7):bqad088.

22. Wangler LM, Godbout JP. Microglia moonlighting after traumatic brain injury: aging and interferons influence chronic microglia reactivity. Trends Neurosci. 2023 Nov;46(11):926–40.

23. Hickman SE, Kingery ND, Ohsumi TK, Borowsky ML, Wang L chong, Means TK, et al. The microglial sensome revealed by direct RNA sequencing. Nat Neurosci. 2013 Dec;16(12):1896–905.

24. Madry C, Attwell D. Receptors, ion channels, and signaling mechanisms underlying microglial dynamics. J Biol Chem. 2015 May 15;290(20):12443–50.

25. Zengeler KE, Lukens JR. Microglia pack a toolbox for life. Trends Immunol. 2024 May;45(5):338–45.

26. Davalos D, Grutzendler J, Yang G, Kim JV, Zuo Y, Jung S, et al. ATP mediates rapid microglial response to local brain injury in vivo. Nat Neurosci. 2005 Jun;8(6):752–8.

27. Nimmerjahn A, Kirchhoff F, Helmchen F. Resting Microglial Cells Are Highly Dynamic Surveillants of Brain Parenchyma in Vivo. Science. 2005 May 27;308(5726):1314–8.

28. Eyo UB, Wu LJ. Microglia: Lifelong patrolling immune cells of the brain. Prog Neurobiol. 2019 Aug;179:101614.

29. Shen K, Pender CL, Bar-Ziv R, Zhang H, Wickham K, Willey E, et al. Mitochondria as Cellular and Organismal Signaling Hubs. Annual Review of Cell and Developmental Biology. 2022 Oct 6;38(Volume 38, 2022):179–218.

30. Collier JJ, Oláhová M, McWilliams TG, Taylor RW. Mitochondrial signalling and homeostasis: from cell biology to neurological disease. Trends Neurosci. 2023 Feb;46(2):137–52.

31. Picard M, Shirihai OS. Mitochondrial signal transduction. Cell Metab. 2022 Nov 1;34(11):1620–53.

32. Tan JX, Finkel T. Mitochondria as intracellular signaling platforms in health and disease. J Cell Biol. 2020 May 4;219(5):e202002179.

33. Kolliniati O, Ieronymaki E, Vergadi E, Tsatsanis C. Metabolic Regulation of Macrophage Activation. J Innate Immun. 2021 Jul 9;14(1):51–68.

34. Mills EL, O'Neill LA. Reprogramming mitochondrial metabolism in macrophages as an anti-inflammatory signal. Eur J Immunol. 2016 Jan;46(1):13–21.

35. Mills EL, Kelly B, Logan A, Costa ASH, Varma M, Bryant CE, et al. Succinate Dehydrogenase Supports Metabolic Repurposing of Mitochondria to Drive Inflammatory Macrophages. Cell. 2016 Oct 6;167(2):457-470.e13.

36. Diskin C, Pålsson-McDermott EM. Metabolic Modulation in Macrophage Effector Function. Front Immunol. 2018;9:270.

37. Ramond E, Jamet A, Coureuil M, Charbit A. Pivotal Role of Mitochondria in Macrophage Response to Bacterial Pathogens. Front Immunol. 2019;10:2461.

38. Wang Y, Li N, Zhang X, Horng T. Mitochondrial metabolism regulates macrophage biology. J Biol Chem. 2021 Jul;297(1):100904.

39. Afroz SF, Raven KD, Lawrence GMEP, Kapetanovic R, Schroder K, Sweet MJ. Mitochondrial dynamics in macrophages: divide to conquer or unite to survive? Biochem Soc Trans. 2023 Feb 27;51(1):41–56.

40. De Biase LM, Schuebel KE, Fusfeld ZH, Jair K, Hawes IA, Cimbro R, et al. Local Cues Establish and Maintain Region-Specific Phenotypes of Basal Ganglia Microglia. Neuron. 2017 Jul 19;95(2):341-356.e6.

41. Maes ME, Colombo G, Schoot Uiterkamp FE, Sternberg F, Venturino A, Pohl EE, et al. Mitochondrial network adaptations of microglia reveal sex-specific stress response after injury and UCP2 knockout. iScience. 2023 Oct 20;26(10):107780.

42. Bordt EA, Moya HA, Jo YC, Ravichandran CT, Bankowski IM, Ceasrine AM, et al. Gonadal hormones impart male-biased behavioral vulnerabilities to immune activation via microglial mitochondrial function. Brain Behav Immun. 2024 Jan;115:680–95.

43. Baik SH, Kang S, Lee W, Choi H, Chung S, Kim JI, et al. A Breakdown in Metabolic Reprogramming Causes Microglia Dysfunction in Alzheimer's Disease. Cell Metabolism. 2019 Sep 3;30(3):493-507.e6.

44. March-Diaz R, Lara-Ureña N, Romero-Molina C, Heras-Garvin A, Ortega-de San Luis C, Alvarez-Vergara MI, et al. Hypoxia compromises the mitochondrial metabolism of Alzheimer's disease microglia via HIF1. Nat Aging. 2021 Apr;1(4):385–99.

45. Fecher C, Trovò L, Müller SA, Snaidero N, Wettmarshausen J, Heink S, et al. Cell-type-specific profiling of brain mitochondria reveals functional and molecular diversity. Nat Neurosci. 2019 Oct;22(10):1731–42.

46. Agarwal A, Wu PH, Hughes EG, Fukaya M, Tischfield MA, Langseth AJ, et al. Transient Opening of the Mitochondrial Permeability Transition Pore Induces Microdomain Calcium Transients in Astrocyte Processes. Neuron. 2017 Feb 8;93(3):587-605.e7.

47. Yona S, Kim KW, Wolf Y, Mildner A, Varol D, Breker M, et al. Fate Mapping Reveals Origins and Dynamics of Monocytes and Tissue Macrophages under Homeostasis. Immunity. 2013 Jan 24;38(1):79–91.

48. Faust TE, Feinberg PA, O'Connor C, Kawaguchi R, Chan A, Strasburger H, et al. A comparative analysis of microglial inducible Cre lines. Cell Rep. 2023 Sep 26;42(9):113031.

49. Bedolla AM, McKinsey GL, Ware K, Santander N, Arnold TD, Luo Y. A comparative evaluation of the strengths and potential caveats of the microglial inducible CreER mouse models. Cell Rep. 2024 Jan 23;43(1):113660.

50. Madisen L, Zwingman TA, Sunkin SM, Oh SW, Zariwala HA, Gu H, et al. A robust and high-throughput Cre reporting and characterization system for the whole mouse brain. Nat Neurosci. 2010 Jan;13(1):133–40.

51. Dietrich MO, Liu ZW, Horvath TL. Mitochondrial Dynamics Controlled by Mitofusins Regulate Agrp Neuronal Activity and Diet-Induced Obesity. Cell. 2013 Sep 26;155(1):188–99.

52. Boldogh IR, Pon LA. Mitochondria on the move. Trends Cell Biol. 2007 Oct;17(10):502–10.

53. Duarte FV, Ciampi D, Duarte CB. Mitochondria as central hubs in synaptic modulation. Cell Mol Life Sci. 2023 Jun 2;80(6):173.

54. Lou N, Takano T, Pei Y, Xavier AL, Goldman SA, Nedergaard M. Purinergic receptor P2RY12-dependent microglial closure of the injured blood-brain barrier. Proc Natl Acad Sci U S A. 2016 Jan 26;113(4):1074–9.

55. Etienne F, Mastrolia V, Maroteaux L, Girault JA, Gervasi N, Roumier A. Two-photon Imaging of Microglial Processes' Attraction Toward ATP or Serotonin in Acute Brain Slices. J Vis Exp. 2019 Jan 31;(143).

56. Bernier LP, York EM, Kamyabi A, Choi HB, Weilinger NL, MacVicar BA. Microglial metabolic flexibility supports immune surveillance of the brain parenchyma. Nat Commun. 2020 Mar 25;11(1):1559.

57. Rock RB, Gekker G, Hu S, Sheng WS, Cheeran M, Lokensgard JR, et al. Role of Microglia in Central Nervous System Infections. Clin Microbiol Rev. 2004 Oct;17(4):942–64.

58. Rodríguez AM, Rodríguez J, Giambartolomei GH. Microglia at the Crossroads of Pathogen-Induced Neuroinflammation. ASN Neuro. 2022 May 29;14:17590914221104566.

59. Norden DM, Trojanowski PJ, Villanueva E, Navarro E, Godbout JP. Sequential activation of microglia and astrocyte cytokine expression precedes increased Iba-1 or GFAP immunoreactivity following systemic immune challenge. Glia. 2016 Feb;64(2):300–16.

60. Nair S, Sobotka KS, Joshi P, Gressens P, Fleiss B, Thornton C, et al. Lipopolysaccharide-induced alteration of mitochondrial morphology induces a metabolic shift in microglia modulating the inflammatory response in vitro and in vivo. Glia. 2019;67(6):1047–61.

61. Park J, Choi H, Min JS, Park SJ, Kim JH, Park HJ, et al. Mitochondrial dynamics modulate the expression of pro-inflammatory mediators in microglial cells. J Neurochem. 2013 Oct;127(2):221–32.

62. Orihuela R, McPherson CA, Harry GJ. Microglial M1/M2 polarization and metabolic states. Br J Pharmacol. 2016 Feb;173(4):649–65.

63. Hu Y, Mai W, Chen L, Cao K, Zhang B, Zhang Z, et al. mTOR-mediated metabolic reprogramming shapes distinct microglia functions in response to lipopolysaccharide and ATP. Glia. 2020 May;68(5):1031–45.

64. O'Neill LAJ, Kishton RJ, Rathmell J. A guide to immunometabolism for immunologists. Nat Rev Immunol. 2016 Sep;16(9):553–65.

65. Van den Bossche J, Baardman J, Otto NA, van der Velden S, Neele AE, van den Berg SM, et al. Mitochondrial Dysfunction Prevents Repolarization of Inflammatory Macrophages. Cell Rep. 2016 Oct 11;17(3):684–96.

66. Hoogland ICM, Houbolt C, van Westerloo DJ, van Gool WA, van de Beek D. Systemic inflammation and microglial activation: systematic review of animal experiments. J Neuroinflammation. 2015 Jun 6;12:114.

67. Su É, Villard C, Manneville JB. Mitochondria: At the crossroads between mechanobiology and cell metabolism. Biology of the Cell. 2023;115(9):e2300010.

68. Picard M, Shirihai OS, Gentil BJ, Burelle Y. Mitochondrial morphology transitions and functions: implications for retrograde signaling? American Journal of Physiology-Regulatory, Integrative and Comparative Physiology. 2013 Mar 15;304(6):R393–406.

69. Candlish M, Hefendehl JK. Microglia Phenotypes Converge in Aging and Neurodegenerative Disease. Front Neurol. 2021;12:660720.

70. Brawek B, Skok M, Garaschuk O. Changing Functional Signatures of Microglia along the Axis of Brain Aging. Int J Mol Sci. 2021 Jan 22;22(3):1091.

71. Niraula A, Sheridan JF, Godbout JP. Microglia Priming with Aging and Stress. Neuropsychopharmacology. 2017 Jan;42(1):318–33.

72. Harrington JS, Ryter SW, Plataki M, Price DR, Choi AMK. Mitochondria in health, disease, and aging. Physiol Rev. 2023 Oct 1;103(4):2349–422.

73. König T, McBride HM. Mitochondrial-derived vesicles in metabolism, disease, and aging. Cell Metab. 2024 Jan 2;36(1):21–35.

74. Moca EN, Lecca D, Hope KT, Etienne F, Schaler AW, Espinoza K, et al. Microglia Drive Pockets of Neuroinflammation in Middle Age. J Neurosci. 2022 May 11;42(19):3896–918.

75. Rangaraju V, Lewis TL, Hirabayashi Y, Bergami M, Motori E, Cartoni R, et al. Pleiotropic Mitochondria: The Influence of Mitochondria on Neuronal Development and Disease. J Neurosci. 2019 Oct 16;39(42):8200–8.

76. Weinberg SE, Sena LA, Chandel NS. Mitochondria in the Regulation of Innate and Adaptive Immunity. Immunity. 2015 Mar 17;42(3):406–17.

77. Zehnder T, Petrelli F, Romanos J, De Oliveira Figueiredo EC, Lewis TL, Déglon N, et al. Mitochondrial biogenesis in developing astrocytes regulates astrocyte maturation and synapse formation. Cell Rep. 2021 Apr 13;35(2):108952.

78. Alshial EE, Abdulghaney MI, Wadan AHS, Abdellatif MA, Ramadan NE, Suleiman AM, et al. Mitochondrial dysfunction and neurological disorders: A narrative review and treatment overview. Life Sci. 2023 Dec 1;334:122257.

79. Norat P, Soldozy S, Sokolowski JD, Gorick CM, Kumar JS, Chae Y, et al. Mitochondrial dysfunction in neurological disorders: Exploring mitochondrial transplantation. NPJ Regen Med. 2020 Nov 23;5(1):22.

80. Fairley LH, Lai KO, Wong JH, Chong WJ, Vincent AS, D'Agostino G, et al. Mitochondrial control of microglial phagocytosis by the translocator protein and hexokinase 2 in Alzheimer's disease. Proc Natl Acad Sci U S A. 2023 Feb 21;120(8):e2209177120.

81. Hope KT, Hawes IA, Moca EN, Bonci A, De Biase LM. Maturation of the microglial population varies across mesolimbic nuclei. Eur J Neurosci. 2020 Oct;52(7):3689–709.

82. Madan S, Uttekar B, Chowdhary S, Rikhy R. Mitochondria Lead the Way: Mitochondrial Dynamics and Function in Cellular Movements in Development and Disease. Front Cell Dev Biol. 2021;9:781933.

83. Banks WA, Robinson SM. Minimal penetration of lipopolysaccharide across the murine blood-brain barrier. Brain Behav Immun. 2010 Jan;24(1):102–9.

84. Banks WA, Gray AM, Erickson MA, Salameh TS, Damodarasamy M, Sheibani N, et al. Lipopolysaccharide-induced blood-brain barrier disruption: roles of cyclooxygenase, oxidative stress, neuroinflammation, and elements of the neurovascular unit. J Neuroinflammation. 2015 Nov 25;12:223.

85. Hasegawa-Ishii S, Inaba M, Shimada A. Widespread time-dependent changes in tissue cytokine concentrations in brain regions during the acute phase of endotoxemia in mice. Neurotoxicology. 2020 Jan;76:67–74.

86. York EM, LeDue JM, Bernier LP, MacVicar BA. 3DMorph Automatic Analysis of Microglial Morphology in Three Dimensions from Ex Vivo and In Vivo Imaging. eNeuro. 2018 Dec 10;5(6):ENEURO.0266-18.2018.

87. Arshadi C, Günther U, Eddison M, Harrington KIS, Ferreira TA. SNT: a unifying toolbox for quantification of neuronal anatomy. Nat Methods. 2021 Apr;18(4):374–7.

88. Gu Z, Eils R, Schlesner M. Complex heatmaps reveal patterns and correlations in multidimensional genomic data. Bioinformatics. 2016 Sep 15;32(18):2847–9.

89. Wickham H. ggplot2 [Internet]. Cham: Springer International Publishing; 2016 [cited 2024 May 17]. (Use R!). Available from: http://link.springer.com/10.1007/978-3-319-24277-4